Chapter 6: TRIBOLOGICAL BEHAVIOUR OF Ni ALLOY-BASED COMPOSITES CONTAINING FIXED AMOUNT OF Ag, AND DIFFERENT AMOUNTS OF *h*-BN-Ni

The chapter begins with the presentation of results on the characterization of Ni doped *h*-BN and ball-milled powders, which is followed by the microstructural, physical, mechanical properties, and characterization of Ni alloy-based composites containing a different amount of Ni-doped *h*-BN (2, 4, 6, and 8 wt.%) and a fixed amount of Ag (10 wt.%). The chapter further presents the tribo-performance evaluation results of above-mentioned composites, along with the microscopic features of the worn surfaces of composites and the counterface Si_3N_4 slid against them. The results have been discussed to understand their tribological behaviour and reveal the prevailing wear mechanisms.

6.1 RESULTS

6.1.1 Characterization of Materials

6.1.1.1 FTIR Spectra of h-BN, h-BN-O, and h-BN-O-Ni

The FTIR spectra of *h*-BN, *h*-BN-O, and *h*-BN-O-Ni depicted in Fig. 6.1 exhibit two distinctive structural vibrations. Two in-plane optical phonon modes (longitudinal and transverse) due to stacked B-N lamellae overlapped with each other and a characteristic strong and broad vibration at ~1400 cm^{-1} in all samples. The out-of-plane B-N-B vibration, also known as buckling mode, is observed at 805 cm^{-1} [103]. The broadening of the B-N-B vibration in *h*-BN-O-Ni is attributed to the deposition of nickel nanoparticles on the surface of *h*-BN-O. A broader peak at ~3400 cm^{-1} in FTIR spectra of *h*-BN and *h*-BN-O attributing to O-H stretches are associated with hydroxyl, and adsorbed water molecules [104]. The hydroxyl functionalities are eliminated to a significant extent during the preparation of *h*-BN-O-Ni in the presence of the strong reducing agent. Consequently, an FTIR spectrum of *h*-BN-O-Ni (Fig. 6.1 (a)) exhibits poor vibrational mode at ~3400 cm^{-1}. The presence of Ni nanoparticles in *h*-BN-O-Ni is confirmed by Ni-O vibration at 472 cm^{-1} in the FTIR spectrum (Fig. 6.1 (b)) of *h*-BN-O-Ni [105].

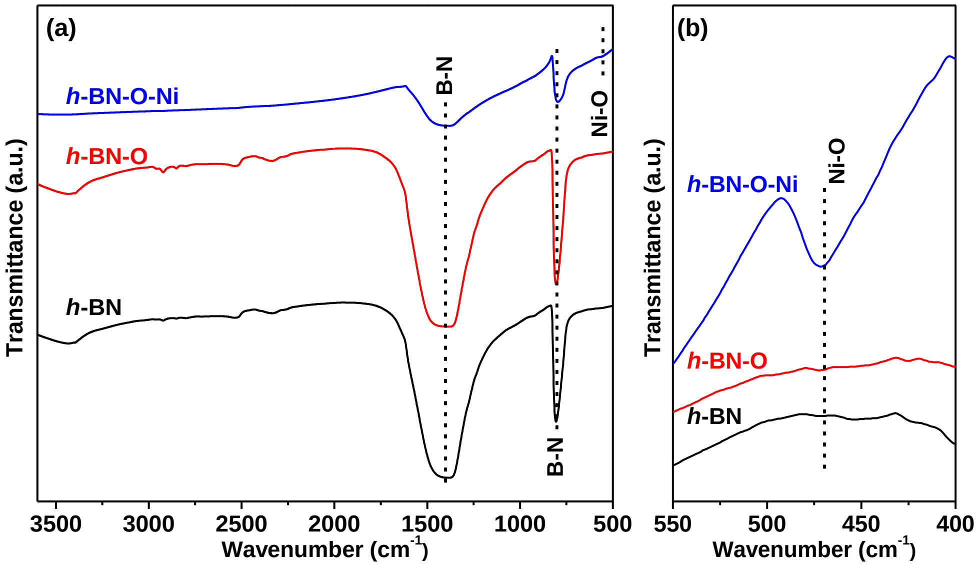

Fig. 6. 1 FTIR spectra of *h*-BN, *h*-BN-O, and *h*-BN-O-Ni along with the assignment of vibrational peaks

6.1.1.2 XRD analysis of h-BN, h-BN-O, and h-BN-O-Ni

The crystalline features including the lamellar pattern of *h*-BN, *h*-BN-O, and *h*-BN-O-Ni have been assessed by their XRD patterns shown in Fig. 6.2. An intense diffraction peak at 2θ of 26.8° corresponding to the (002) plane signifies an interlamellar spacing of 0.33 nm. It also exhibits a few more peaks at 2θ of 41.5, 50.1, 55.1, 76.0, and 82.1° revealing the (100), (102), (004), (110), and (112) planes of *h*-BN and confirm the lamellar pattern in *h*-BN nano powder. These diffraction peaks are also observed in *h*-BN-O and *h*-BN-O-Ni without any shift in their positions, confirming that crystalline features of *h*-BN have remained intact in both the *h*-BN-O and *h*-BN-O-Ni [103,104]. New diffraction peaks at 2θ of 44.4, 51.7, and 92.9° corresponding to the (111), (002), and (311) lattice planes of metallic nickel seen in the XRD pattern of *h*-BN-O-Ni, confirm the deposition of crystalline Ni nanoparticles on the surface of *h*-BN-O [106]. The appearance of a weak diffraction peak at 2θ of 33.2° associated with the (100) plane of nickel hydroxides indicates the minute presence of $Ni(OH)_2$ accompanying the metallic nickel [107].

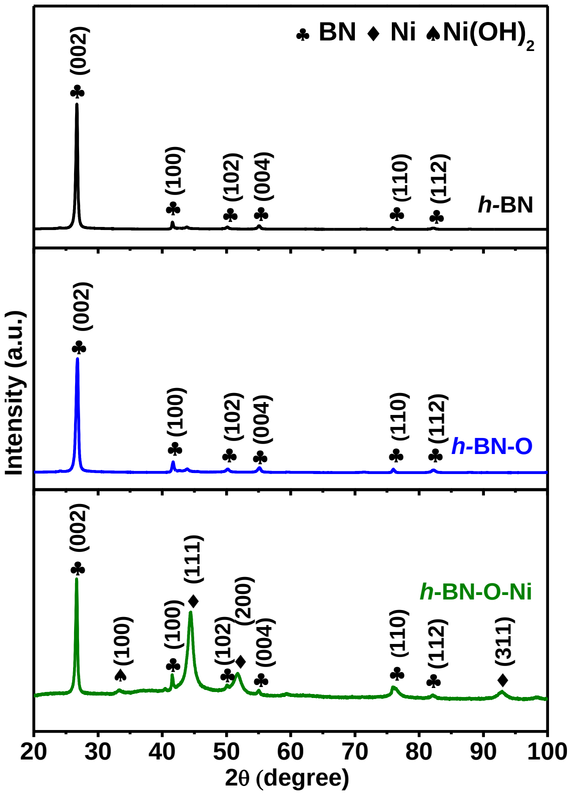

Fig. 6. 2 XRD patterns (a) *h*-BN, (b) *h*-BN-O, and (c) *h*-BN-O-Ni, along with the assignment of diffraction features

6.1.1.3 TEM analysis of h-BN-O-Ni

Figures 6.3 (a and b) illustrate the TEM micrographs of *h*-BN-O-Ni revealing the sheets of different size. The contrast difference in these micrographs is attributed to the aggregation and stacking of *h*-BN sheets. The spherical Ni nanoparticles could be explicitly seen (indicated by black arrows) in a high-resolution micrograph of *h*-BN-O-Ni given as Fig. 6.3 (b). These nanoparticles with a diameter of 3-7 nm are regularly distributed on the surface of *h*-BN nanosheets. The elemental mapping of the *h*-BN-O-Ni shows the regular distribution of B, N, O, and Ni as seen from Fig. 6.3 (c), revealing the thorough distribution of Ni nanoparticles on the oxidized nanosheets of *h*-BN in the *h*-BN-O-Ni.

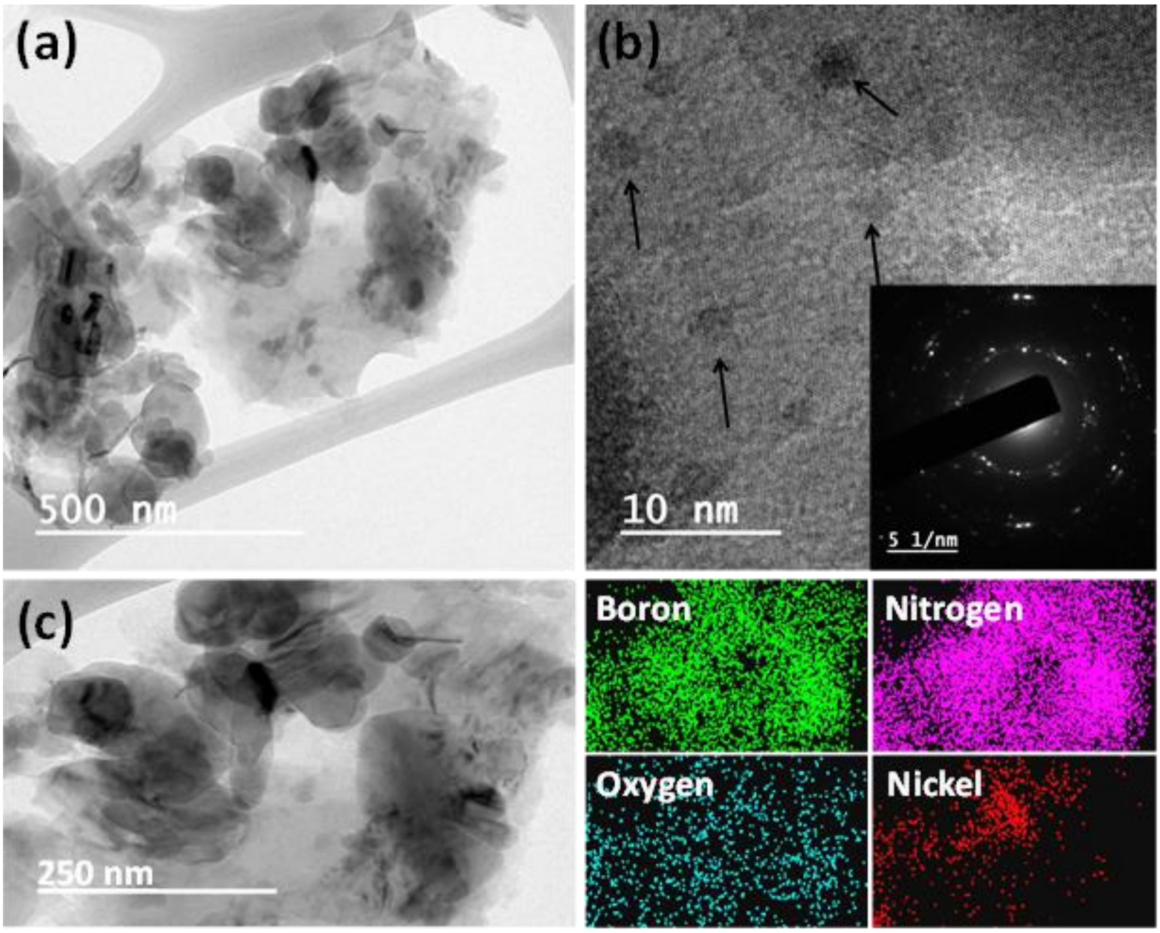

Fig. 6. 3 TEM images of *h*-BN-O-Ni at (a) low and (b) high magnifications. The nickel-based nanoparticles (indicated by black arrows) in a range of 2-4 nm are distributed on *h*-BN-O nanosheets. The SAED pattern with crystalline fringes of *h*-BN-O-Ni is shown as an inset of (b). (c) Micrograph of *h*-BN-O-Ni along with corresponding area elemental (B, N, O, and Ni) distribution based on EDS measurements.

6.1.1.4 XPS analysis of h-BN-O and h-BN-O-Ni

The XPS survey spectrum of *h*-BN-O presented in Fig. 6.4 (a) exhibits spectral features associated with C, B, N, and O, whereas the spectrum of *h*-BN-O-Ni shows additional peaks corresponding to Ni as seen from Fig. 6.4 (b). The high-resolution spectra of B 1s, C 1s, N 1s, O 1s, and Ni 2p for both the *h*-BN-O and *h*-BN-O-Ni are collected and fitted into chemically shifted peak components for revealing the surface composition. The B 1s spectrum of *h*-BN-O exhibits two peaks as shown in Fig. 6.5 (a). An intense B 1s peak component at 190.2 eV signifies the B-N linkages-based *h*-BN network, whereas B 1s peak component at a higher binding energy (191.4 eV) with a significantly low intensity suggests the B-O linkage-based oxygen functionalities in the *h*-BN-O [108,109]. The B 1s spectrum of *h*-BN-O-Ni also shows similar spectral features attributed to B-N and B-O linkages (Fig. 6.5 (f)). The C 1s spectra of *h*-BN-O and *h*-BN-O-Ni given in Figs. 6.5 (b and g) comprising peak components of C-C/C-H, C-O, and COO-based functionalities/linkages represent the adventitious carbon adsorbed on the surface of these materials. The N 1s spectra of the *h*-BN-O and *h*-BN-O-Ni (Figs. 6.5 (c and h)) at 397.7 eV with an intense peak signify N-B based linkages of *h*-BN nanosheets in both materials. A very poor peak component at 398.8 eV has revealed the N-H linkages in both the *h*-BN-O and *h*-BN-O-Ni. The high-resolution O 1s spectrum of the *h*-BN-O shows three peak components at 531.8, 532.5, and 533.3 eV attributed to the O-H, O-B, and O-C linkages based functional groups (Fig. 6.5 (d)), whereas the O 1s spectrum of *h*-BN-O-Ni (Fig. 6.5 (i)) exhibits an additional major peak component at 530.5 eV revealing the Ni-O linkages of nickel nanoparticles decorated on the surface of the *h*-BN nanosheets [110,111]. The high-resolution Ni 2p spectrum of the *h*-BN-O-Ni shows two major peaks at 855.2 and 872.7 eV, representing the doublet of Ni $2p_{3/2}$ and Ni $2p_{1/2}$, respectively, with a spin-orbit difference of 17.5 eV (Fig. 6.5 (j)). The Ni 2p doublet also exhibits corresponding broader satellite peaks at 816.2 and 879.1 eV. A further fitting of Ni $2p_{3/2}$ and Ni $2p_{1/2}$ peaks has revealed the presence of dual states of nickel nanoparticles, i.e., Ni (0) and Ni (II). The Ni $2p_{3/2}$ peak at 852.8 eV suggests pure metallic nickel [Ni (0)], whereas the existence of peak component at higher binding energies (854.8 and 855.8 eV) signifies the oxygenated form of nickel, i.e., NiO and $Ni(OH)_2$ [112,113] . The area ratio between the Ni $2p_{1/2}$ and Ni $2p_{3/2}$ is estimated to be 2.7, which is closer to the theoretical ratio of 1:3. The higher intensity of oxygen-based Ni (II) functionalities indicates the partial oxidative forms on the surface of nickel nanoparticles due to their exposure to air.

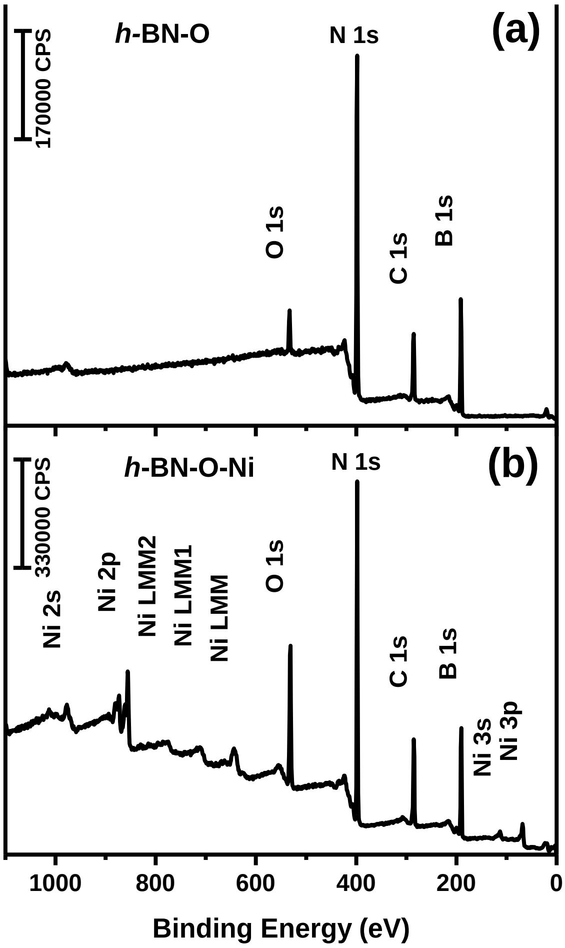

Fig. 6. 4 Survey spectra of (a) *h*-BN-O and (b) *h*-BN-O-Ni along with assignment of spectral features

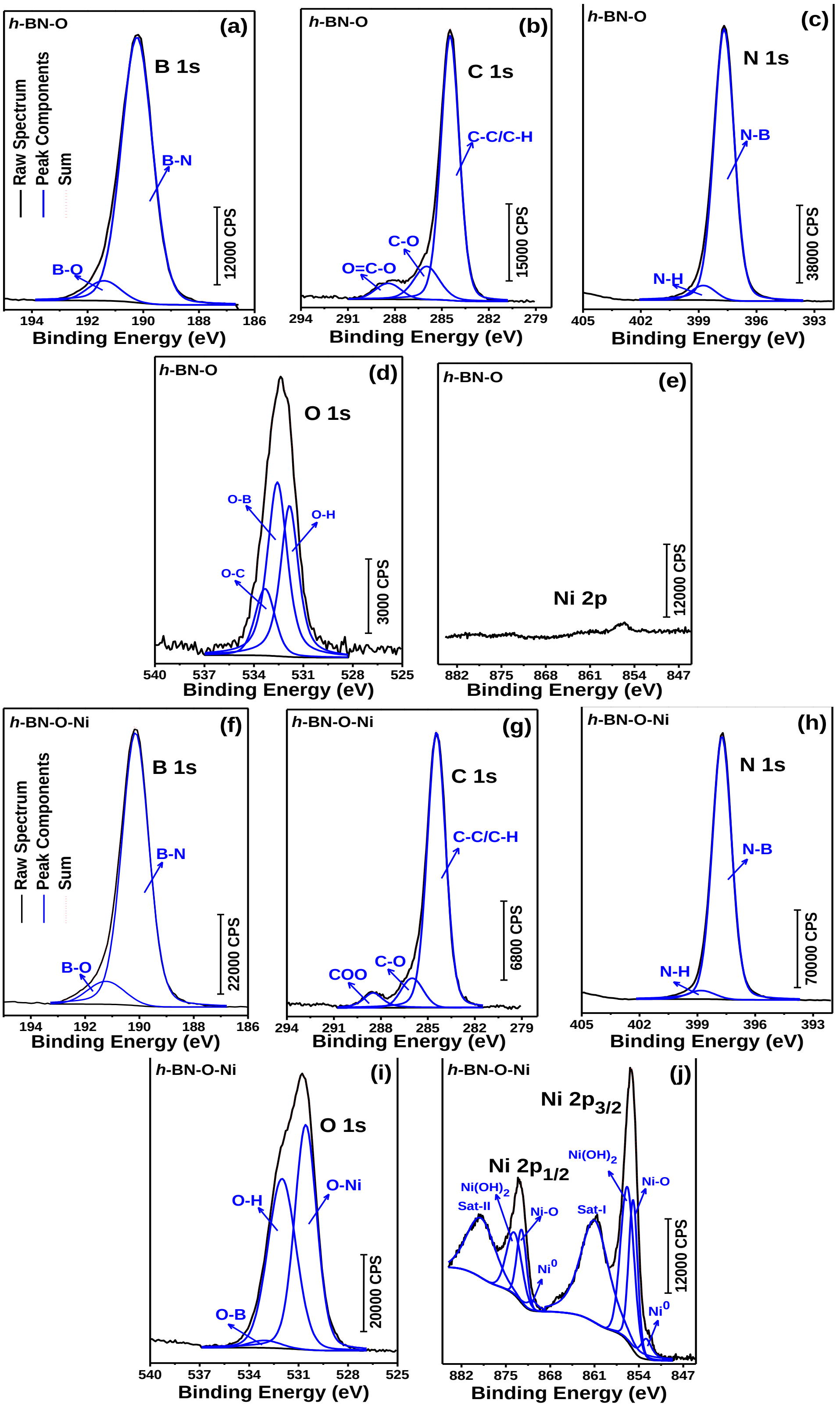

Fig. 6. 5 High-resolution (a) B 1s, (b) C 1s, (c) N 1s (d) O 1s, and (e) Ni 2p XP spectra along with deconvoluted peak components of *h*-BN-O. (f) B 1s, (g) C 1s, (h) N 1s, (i) O 1s, and (j) Ni 2p XP spectra along with deconvoluted peak components of *h*-BN-O-Ni

6.1.1.5 Morphology of ball-milled powders and composites

The fragmentation of flattened particles has been found to occur in milled powders for all. The average size of flattened particles decreases from 50.1 to 41.2 µm with an increase in the amount from 0.5 to 2.0 wt.% of rGO as seen by a comparison of Figs. 6.6 (a-d).

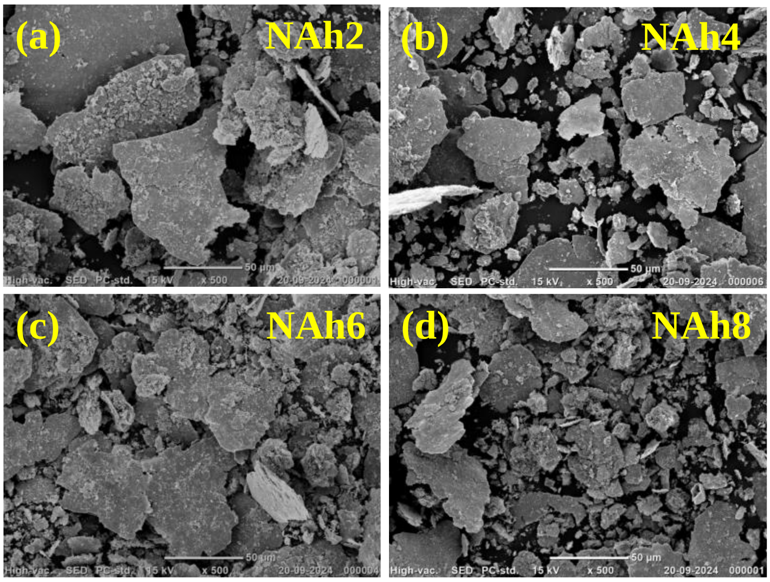

Fig. 6. 6 FESEM images of milled powders (a) NAh2, (b) NAh4, (c) NAh6, and (d) NAh8

6.1.1.6 X-ray diffraction analysis of ball-milled powders and composites

The XRD patterns shown in Figs. 6.7 (a) and (b) reveal the crystalline features of powder mixtures and sintered composites, respectively. The diffraction peaks at 2θ of ~ 44.40 and 76.31° corresponding to the (111), and (022) planes of Ni (ICSD 98-026-0169 could be observed in Fig. 6.7 (a) apart from peaks pertaining to Cr and Mo. The diffraction peaks at 2θ of ~51.76, 64.79, 81.68, and 93.10° have been found to correspond with (002), (200), (211), and (220) planes of Cr (ICSD 00-006-0694). The peaks at 2θ of ~40.57, 58.69, and 73.54° have been attributed to (011), (002), and (112) planes of Mo (ICSD 98-017-3127) and at ~ 40.52° pertains to the (011) plane of Ti (ICSD 98-009-9778). One may also observe the additional peaks corresponding to Ag at ~38.15 and 81.64°, which have been assigned to the (111) and (222) planes of the Ag in the powder mixture of NA. However, an additional peak corresponding to *h*-BN (ICSD 01-085-1068) in the XRD patterns of powder mixtures of NAh2, NAh4, NAh6, and NAh8 could be seen at 2θ of 88.96°.

The XRD pattern of sintered base alloy (N0) and composites shown in Fig. 6.7 (b) reveal the peaks at 2θ of ~ 42.04, 45.34, and 76.95° corresponding to the (111), (012), and (022) planes of Ni and belonging to (002), (200), and (220) planes of Cr at 2θ of ~ 49.66, 63.55, and 91.03°. The peak at 2θ of ~74.23° corresponds to the (122) plane of Mo, whereas the peak at ~36.89° pertains to the (011) plane of Ti (ICSD 98-009-9778). The XRD pattern of NA reveals the presence of the additional peaks at ~36.88 and 80.76° corresponding to (111) and (222) planes Ag. However, the composites containing Ag and *h*-BN, i.e., NAh2, NAh4, NAh6, and NAh8 show the peaks pertaining to *h*-BN at 2θ of ~28.1 and 72.59 ºC in the XRD spectrum as shown in Fig. 6.7 (b). X-ray diffraction patterns of sintered base alloy and composites affirm that no oxidation has taken place during the sintering of the powders under vacuum conditions.

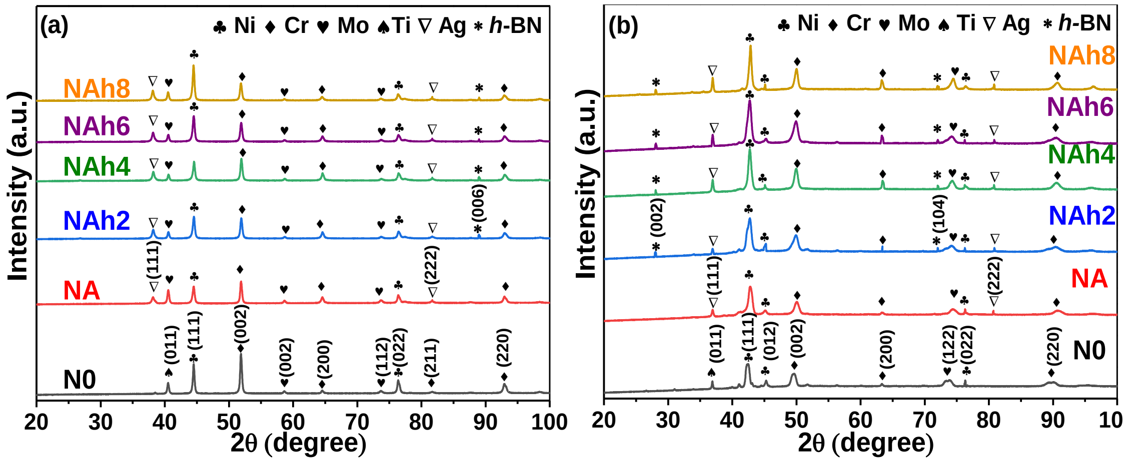

Fig. 6. 7 X-ray diffraction patterns of (a) ball milled powder and (b) spark plasma sintered base alloy and composites

6.1.1.7 Microstructural analysis

The microstructure with area elemental mapping for the composites having 2, 4, 6, and 8 wt.% *h*-BN, i.e., NAh2, NAh4, NAh6, and NAh8, respectively, has been shown in Fig. 6.8. The micrographs showing the microstructure for N0 and NA have already been presented in Figs. 4.8 (a and b),hence not shown here. The light grey regions of Ag in the composite having 2 wt.% *h*-BN, i.e., NAh2 could be seen in Fig. 6.8(a), and these regions decrease in size with an increase in the amount of *h*-BN. However, the existence of pores can be seen in the microstructure of the composite having 8 wt.% *h*-BN. One may observe the nearly homogeneous distribution of *h*-BN for relatively lower addition of *h*-BN, i.e., 2 and 4 wt.% as seen from Figs. 6.8 (a and b). This may also be judged from the area elemental mapping of NAh4 which exhibits the uniform distribution of the constituent elements in comparison to others. However, the agglomeration of *h*-BN has been found to occur in NAh6 and NAh8 containing 6 and 8 wt.% *h*-BN, respectively, as seen in Figs. 6.8 (c and d). EDS analysis of the marked regions of NAh8 shown in Fig. 6.9 reveals that region 1 is rich in Ti and region 2 is rich in Ni. The same is also reflected in the area elemental mapping of NAh8 as given in Fig. 6.8.

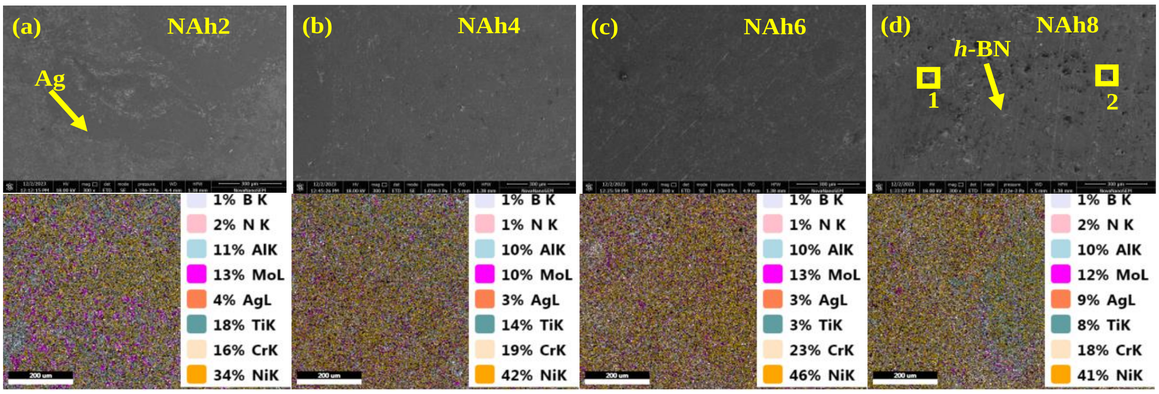

Fig. 6. 8 FESEM micrographs for the microstructure of (a) NAh2, (b) NAh4, (c) NAh6, and (d) NAh8 along with corresponding area elemental distribution

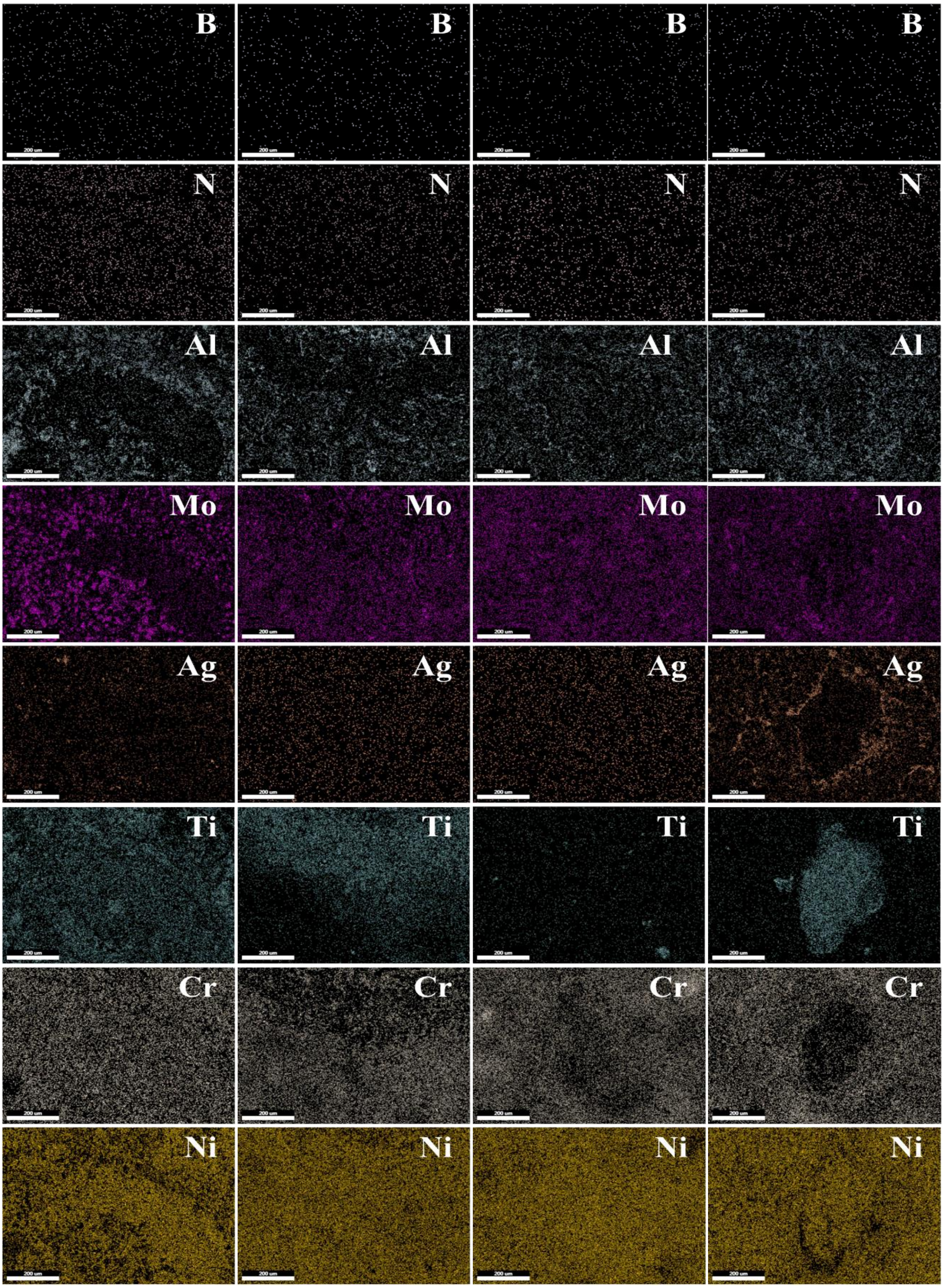
B
200 um
B
200 um
B
200 um
B
200 um
N
200 um
N
200 um
N
200 um
N
200 um
Al
200 um
Al
200 um
Al
200 um
Al
200 um
Mo
200 um
Mo
200 um
Mo
200 um
Mo
200 um
Ag
200 um
Ag
200 um
Ag
200 um
Ag
200 um
Ti
200 um
Ti
200 um
Ti
200 um
Ti
200 um
Cr
200 um
Cr
200 um
Cr
200 um
Cr
200 um
Ni
200 um
Ni
200 um
Ni
200 um
Ni
200 um

Fig. 6.8 Contd.

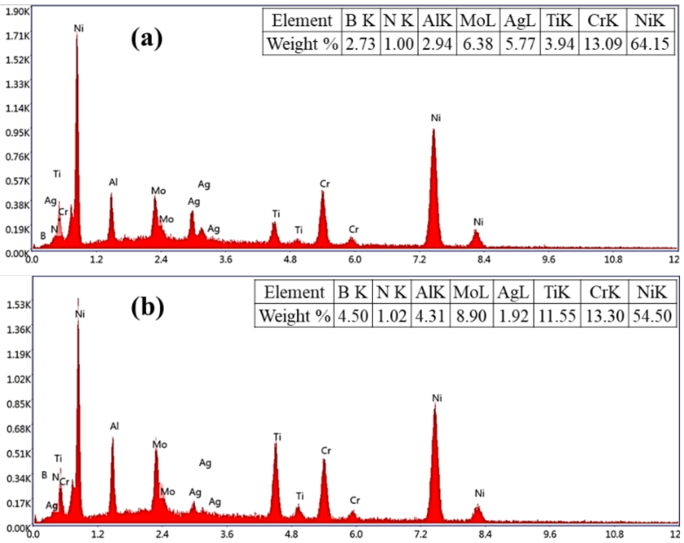

(a)

Element	B K	N K	AlK	MoL	AgL	TiK	CrK	NiK
Weight %	2.73	1.00	2.94	6.38	5.77	3.94	13.09	64.15

(b)

Element	B K	N K	AlK	MoL	AgL	TiK	CrK	NiK
Weight %	4.50	1.02	4.31	8.90	1.92	11.55	13.30	54.50

Fig. 6. 9 EDS of (a) region 1 and (b) region 2 marked in the microstructure of NAh8 in Fig. 6.8 (d)

6.1.1.8 Hardness and density measurement

Table 6.1 presents the specimen designation, composition, and densities, along with their microhardness. One may observe that there is a reduction in both the density and hardness of the base alloy, i.e., N0, with the incorporation of Ag and Ni-doped *h*-BN. The density of the NAh4 has been observed to be relatively higher than other composites, i.e., NAh2, NAh6, and NAh8. The hardness has been found to decrease with increasing amount of *h*-BN in the composites.

Table 6. 1 Specimen designation, composition, density, and microhardness

Designation	Composition	Real density (g/cm^3)	Microhardness HV$_{0.3}$ (GPa)
NAh2	Ni alloy-10 wt.% Ag-2 wt.% *h*-BN	7.13	405 ± 3
NAh4	Ni alloy-10 wt.% Ag-4 wt.% *h*-BN	7.68	354 ± 2
NAh6	Ni alloy-10 wt.% Ag-6 wt.% *h*-BN	7.40	329 ± 1
NAh8	Ni alloy-10 wt.% Ag-8 wt.% *h*-BN	7.08	313 ± 2

6.1.2 Dry Sliding Friction and Wear Behaviour

6.1.2.1 Variation of coefficient of friction with time

The variation of coefficient of friction (CoF) with respect to time for a particular composition at a constant normal load of 5 N at sliding speed of 0.5 m/s has been depicted in Fig. 6.10. The variations of CoF with time at different temperatures for N0 and NA have already been presented and described in Fig 4.11, hence not included here. One may observe a fluctuating trend for all the composites with varying amplitude of fluctuations depending on temperature. The CoF for NAh2 is observed to stabilize after 192, 102, 501, 431, and 98 seconds at RT, 200, 400, 600, and 800 °C, respectively, with comparatively larger fluctuations at RT and 800 °C than at other temperatures as shown in Fig. 6.10 (a). The CoF for NAh4 has been found to stabilize after 412, 352, 801, 214, and 125 seconds at RT, 200, 400, 600, and 800 °C, respectively, with comparatively smaller fluctuations at 200 and 600 °C than at other temperatures as seen from Fig. 6.10 (b). The CoF for NAh6 is found to stabilize after 415, 388, 417, 192, and 198 seconds at RT, 200, 400, 600, and 800 °C, respectively, with relatively larger fluctuations at RT and 800 °C than at other temperatures as depicted in Fig. 6.10 (c). The CoF for NANh8 is observed to stabilize after 601, 148, 254, 210, and 352 seconds at RT, 200, 400, 600, and 800 °C, respectively, with comparatively larger fluctuations at 600 and 800 °C than at other temperatures as shown in Fig. 6.10 (d).

6.1.2.2 Variation of average coefficient of friction with temperature

Figure 6.11 illustrates the variation of average CoF, estimated by discarding the running-in period, with temperature. One may observe that the CoF for N0 decreases with increasing temperature from RT to 800 °C. However, the decrease is relatively sharp from RT to 200 °C and 600 to 800 °C. A similar trend in the variation of CoF could also be seen for NA, NAh2, and NAh4 from RT to 800 °C. The CoF for NAh6 is observed to decrease continuously from RT to 800 °C, with relatively large decrement from 600 to 800 °C. NAh8 also exhibits a decreasing trend of CoF with an increase in temperature. However, the decrease is relatively steep from 200 to 400 °C and 600 to 800 °C. It may be noted that the CoF at a particular temperature for base alloy, NA, and composites decreases follows the given order: N0>NA > NAh2> NAh4> NAh6>NAh8.

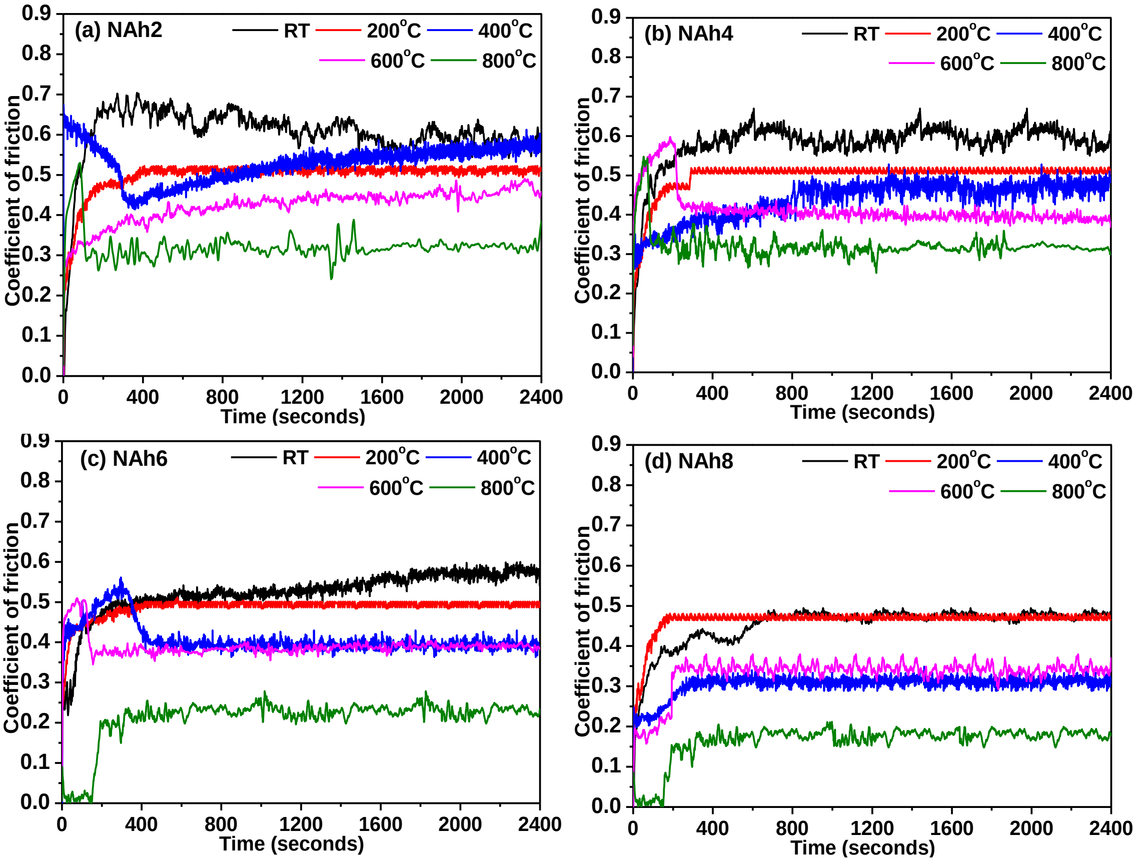

Fig. 6. 10 Variation of coefficient of friction with time for (a) NAh2, (b) NAh4, (c)NAh6, and (d) NAh8 at all the temperatures

6.1.2.3 Variation of wear rate with temperature

The variation of specific wear rate with temperature for N0 and composites is shown in Fig. 6.12. The specific wear rate for base alloy has been observed to increase from RT to 600 °C with a slight reduction thereafter at 800 °C. The wear rate for the composites, i.e., NA, NAh2, NAh4, NAh6, and NAh8 has been found to increase from RT to 400 °C, which is followed by a decrease at 600 and 800 °C. However, an increase from 200 to 400 °C and a decrease from 600 to 800 °C are relatively sharp in all the composites. It may be noted that the wear rate of the base alloy (N0) has been observed to decrease significantly after addition of 10 wt. % Ag (NA) at all the temperatures. The wear rate of NA has been found to reduce further with the addition of 2 and 4 wt.% *h*-BN. However, the wear rate has been observed to increase after addition of relatively larger amounts (6 and 8 wt. %) of *h*-BN. The wear rate for NAh6 containing a combination of 10 wt.% Ag and 6 wt.% *h*-BN has been found to lie in-between N0 and NA at all the temperatures. The composite containing 10 wt.% Ag and 8 wt.% *h*-BN i.e., NAh8 has shown the highest wear rate among all the composites at all the temperatures. The wear rate shown by NAh8 is even higher than N0 at RT, 200 and 400 °C whereas it is almost the same at 600 and 800 °C. This may possibly be the result of the reduced hardness due to addition of higher amount of *h*-BN and its agglomeration in the composites.

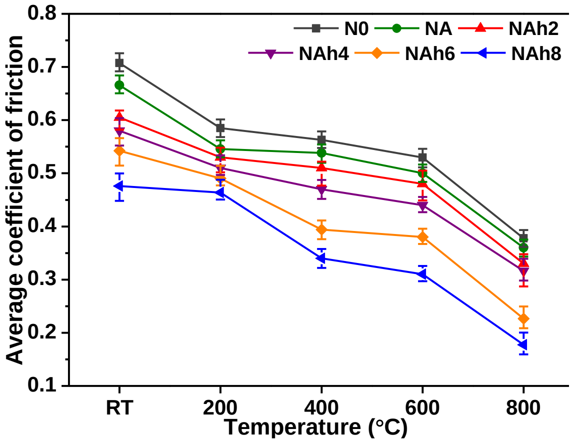

Fig. 6. 11 Variation of average coefficient of friction for base alloy and composites with temperature

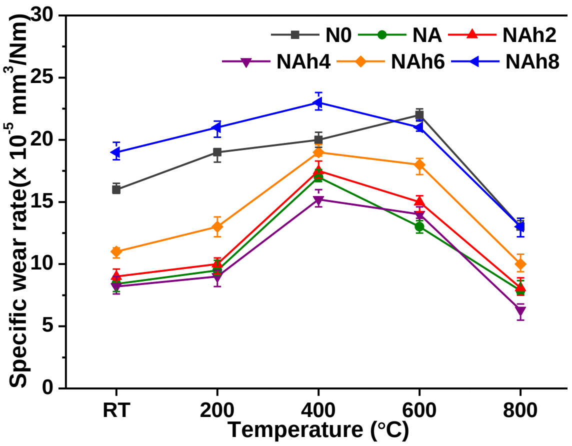

Fig. 6. 12 Variation of specific wear rate for the base alloy and composites with temperature

6.1.3 Analysis of Worn Surfaces

6.1.3.1 Electron microscopy of worn surfaces of tribo-pairs

The FESEM micrographs of the worn surfaces of N0, NA, and the balls at different temperatures have already been presented and discussed in detail in Chapter 4. The worn surfaces of N0 revealed the existence of a transfer layer, ploughing marks, loose wear particles and delamination depending on the temperatures. The worn surface of the ball slid against N0 exhibited the presence of loose wear particles scattered on the surface and a transfer layer with varied degrees of compaction and area coverage based on the temperature of testing. The FESEM micrographs of the worn surface of NA after the tribo-tests showed a smooth surface, ploughing marks, and loosely bound or compacted transfer layer depending on temperature. The worn surface of the counterface slid against NA revealed similar features as seen on the worn surface of the ball slid against N0.

The FESEM micrographs of the worn surfaces of NAh2 at RT, 200, 400, 600, and 800 °C, along with the EDS analyses of the regions marked by the square are shown in Figs. 6.13 (a-j). The worn surface of NAh2 has revealed some deeper ploughing marks covered by a transfer layer after sliding at RT as seen from Fig. 6.13 (a). However, the transfer layer does not appear to be continuous. The EDS analysis of the marked region given in Fig. 6.13 (b) shows the presence of oxygen and other constituent elements indicating oxidation at some extent. At 200 °C, the morphology of worn surface of NAh2 exhibits relatively shallow ploughing marks as compared to those observed at RT as seen from a comparison of Figs. 6.13 (a and c). One may also observe the presence of a transfer layer at several locations partially covering the ploughing marks as seen in Fig. 6.13 (c). In contrast to this, loose wear debris and a scattered transfer layer could be seen on the surface worn at 400 °C, whereas the surface worn at 600 °C exhibits the regions of delamination along the transfer layer as depicted in Figs. 6.13 (e and g). However, the worn surface at 800 °C reveals the existence of a smooth transfer layer (Fig. 6.13 (i)). The EDS analyses of the square regions marked in Figs. 6.13 (c, e, g, and i) reveal the presence of constituent elements of the composite and oxygen along with their respective amounts depending on the temperature indicating towards the possibility of oxidation as seen from Figs. 6.13 (d, f, h, and j).

Figures 6.14 (a-f) illustrate the morphology of the worn surfaces of the ball slid against NAh2 after the tribo-tests at RT, 400, and 800 °C, along with their EDS analyses. The presence of loose wear debris could be observed on the worn surface of ball at different temperatures. However, the quantity of debris adhered to the worn surface at 400 °C is observed to be more than that at RT as seen from a comparison to Figs. 6.14 (a and c). At 800 °C, the worn surface of ball shows the presence of a compacted layer of wear debris which appears to be on the verge of spalling, apart from loose wear particles as seen in Fig. 6.14 (e). The EDS analysis of the regions marked by square on the worn surface of the ball given in Figs. 6.14 (b, d, and f) reveal the transfer of material from the composite to the ball and the presence of oxygen points towards the oxidation of elements.

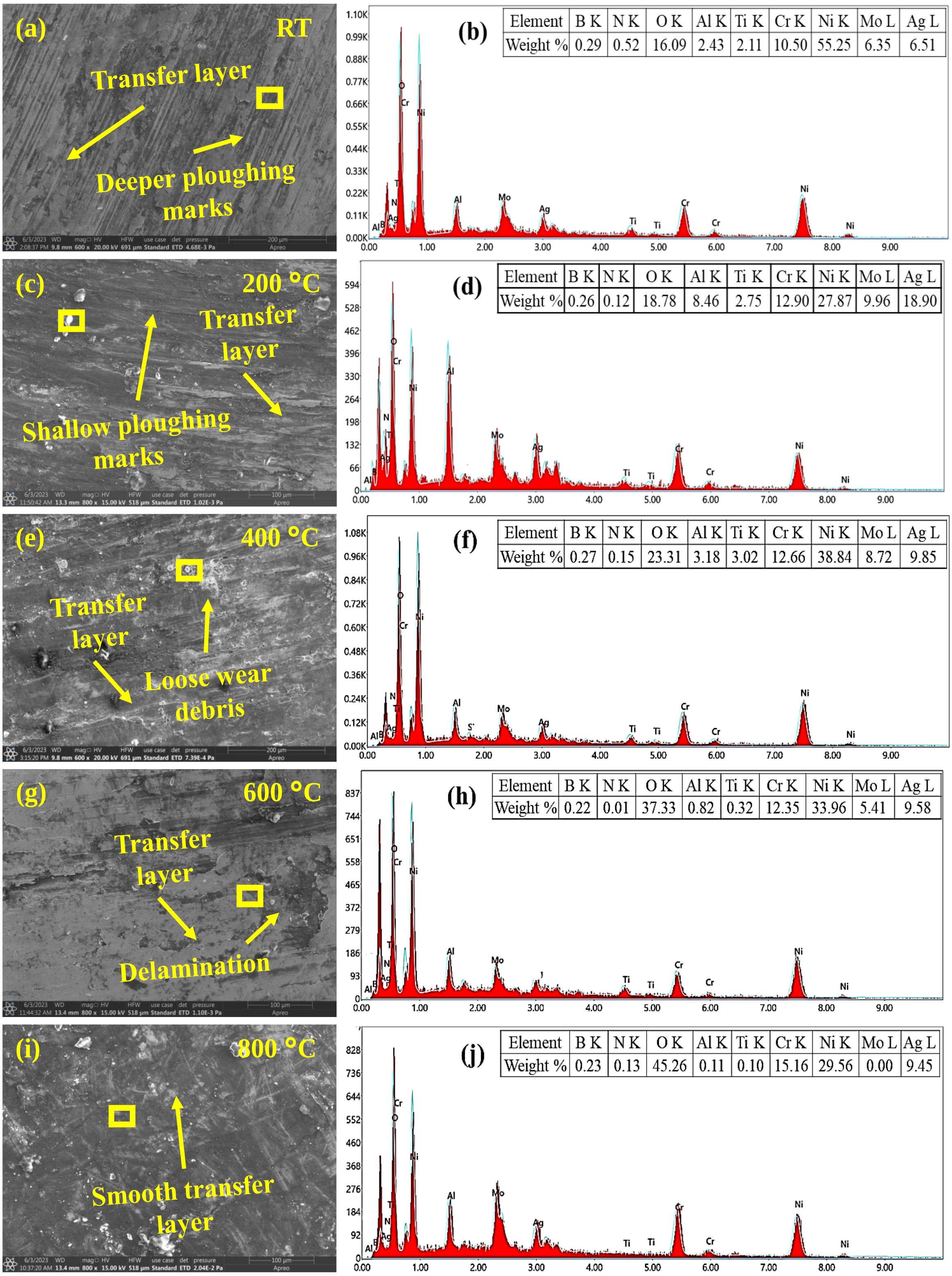

(b)

Element	B K	N K	O K	Al K	Ti K	Cr K	Ni K	Mo L	Ag L
Weight %	0.29	0.52	16.09	2.43	2.11	10.50	55.25	6.35	6.51

(d)

Element	B K	N K	O K	Al K	Ti K	Cr K	Ni K	Mo L	Ag L
Weight %	0.26	0.12	18.78	8.46	2.75	12.90	27.87	9.96	18.90

(f)

Element	B K	N K	O K	Al K	Ti K	Cr K	Ni K	Mo L	Ag L
Weight %	0.27	0.15	23.31	3.18	3.02	12.66	38.84	8.72	9.85

(h)

Element	B K	N K	O K	Al K	Ti K	Cr K	Ni K	Mo L	Ag L
Weight %	0.22	0.01	37.33	0.82	0.32	12.35	33.96	5.41	9.58

(j)

Element	B K	N K	O K	Al K	Ti K	Cr K	Ni K	Mo L	Ag L
Weight %	0.23	0.13	45.26	0.11	0.10	15.16	29.56	0.00	9.45

Fig. 6. 13 FESEM micrographs of the worn-out NAh2 composite and EDS of the marked region at (a and b) RT, (c and d) 200, (e and f) 400, (g and h) 600, and (i and j) 800 °C

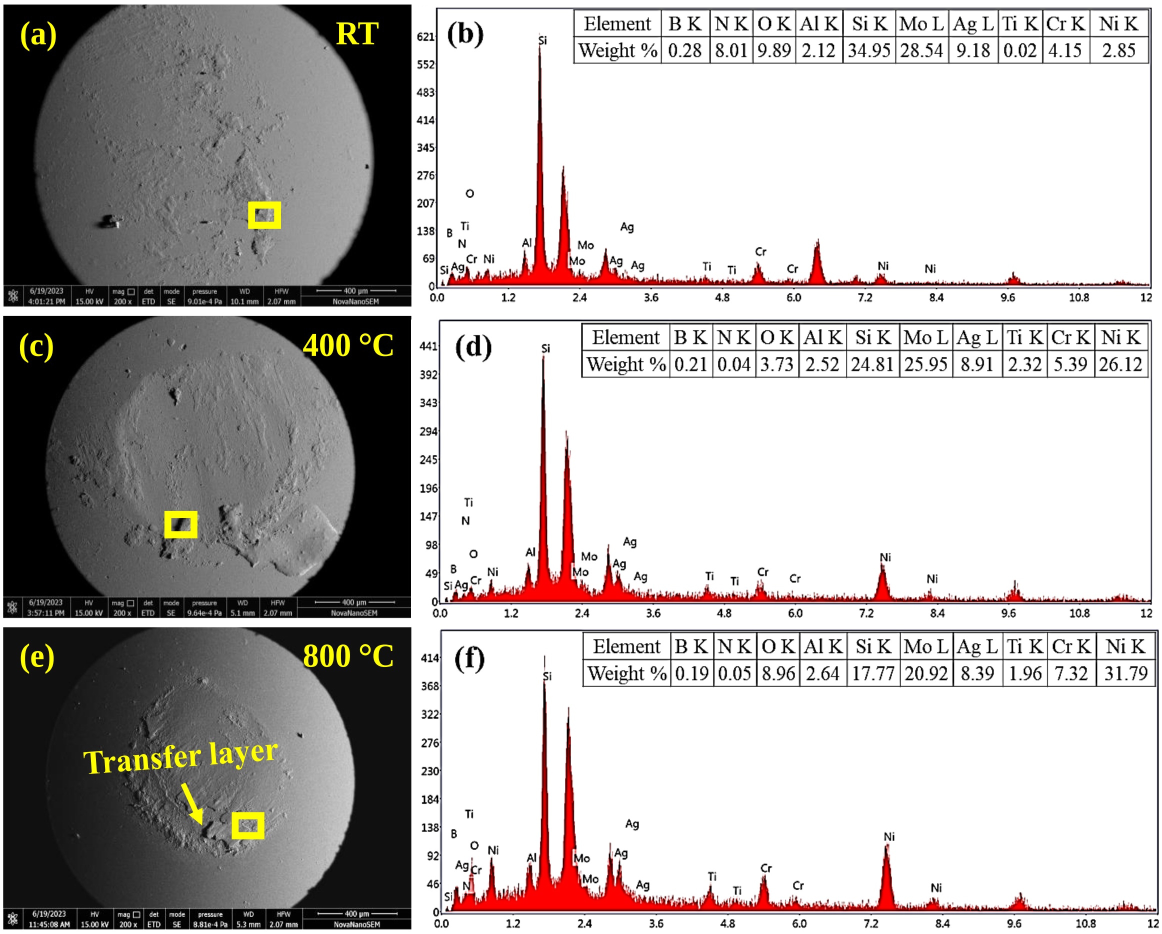

(b)

Element	B K	N K	O K	Al K	Si K	Mo L	Ag L	Ti K	Cr K	Ni K
Weight %	0.28	8.01	9.89	2.12	34.95	28.54	9.18	0.02	4.15	2.85

(d)

Element	B K	N K	O K	Al K	Si K	Mo L	Ag L	Ti K	Cr K	Ni K
Weight %	0.21	0.04	3.73	2.52	24.81	25.95	8.91	2.32	5.39	26.12

(f)

Element	B K	N K	O K	Al K	Si K	Mo L	Ag L	Ti K	Cr K	Ni K
Weight %	0.19	0.05	8.96	2.64	17.77	20.92	8.39	1.96	7.32	31.79

Fig. 6. 14 FESEM micrographs of the worn-out silicon nitride ball (counterface) slid against NAh2 along with EDS at the marked region at (a and b) RT, (c and d) 400, and (e and f) 800 °C

The FESEM micrographs of the worn surfaces of NAh4 at RT, 200, 400, 600, and 800 °C, along with the EDS analyses, are shown in Figs. 6.15 (a-j). The presence of a transfer layer, along with the ploughing marks, can be observed on the worn surface of NAh4 after sliding at RT, as seen in Fig. 6.15 (a). The presence of loose wear debris along with the transfer layer is seen on the worn surface at 200 °C (Fig. 6.15 (c)). In contrast to this, a compacted transfer layer could be seen on the surface worn at 400 and 600 °C, whereas some signs of cracking (marked by arrow) at 600 °C as seen from Figs. 6.15 (e and g). However, a smooth and well-compacted transfer layer could be observed on the worn surface of NAh4 at 800 °C (Fig. 6.15 (i)). The EDS analyses of the square regions marked in Figs. 6.15 (a, c, e, g, and i) reveal the presence of constituent elements of the composite and oxygen along with their respective amounts depending on the temperature indicating the possibility of oxidation as evident from Figs. 6.15 (b, d, f, h, and j).

The morphology of the worn surfaces of the ball slid against NAh4 at RT, 400, and 800 °C and their EDS analyses have been shown in Figs. 6.16 (a-f). One may observe the presence of wear debris apart from sliding marks on the worn surface of the ball at RT, 400, and 800 °C. The wear debris appears to have accumulated at the leading edge of the ball forming either discrete plateau at RT (Fig. 6.16 (a)) or a compacted layer at 400 and 800 °C (Figs. 6.16 (c and e)), respectively. However, the layer appears to be spalling at 400 °C. The EDS analysis of the regions marked by square on the worn surface of the ball given in Figs. 6.16 (b, d, and f) reveal the transfer of material from the composite to the ball and the presence of oxygen points towards the oxidation of elements.

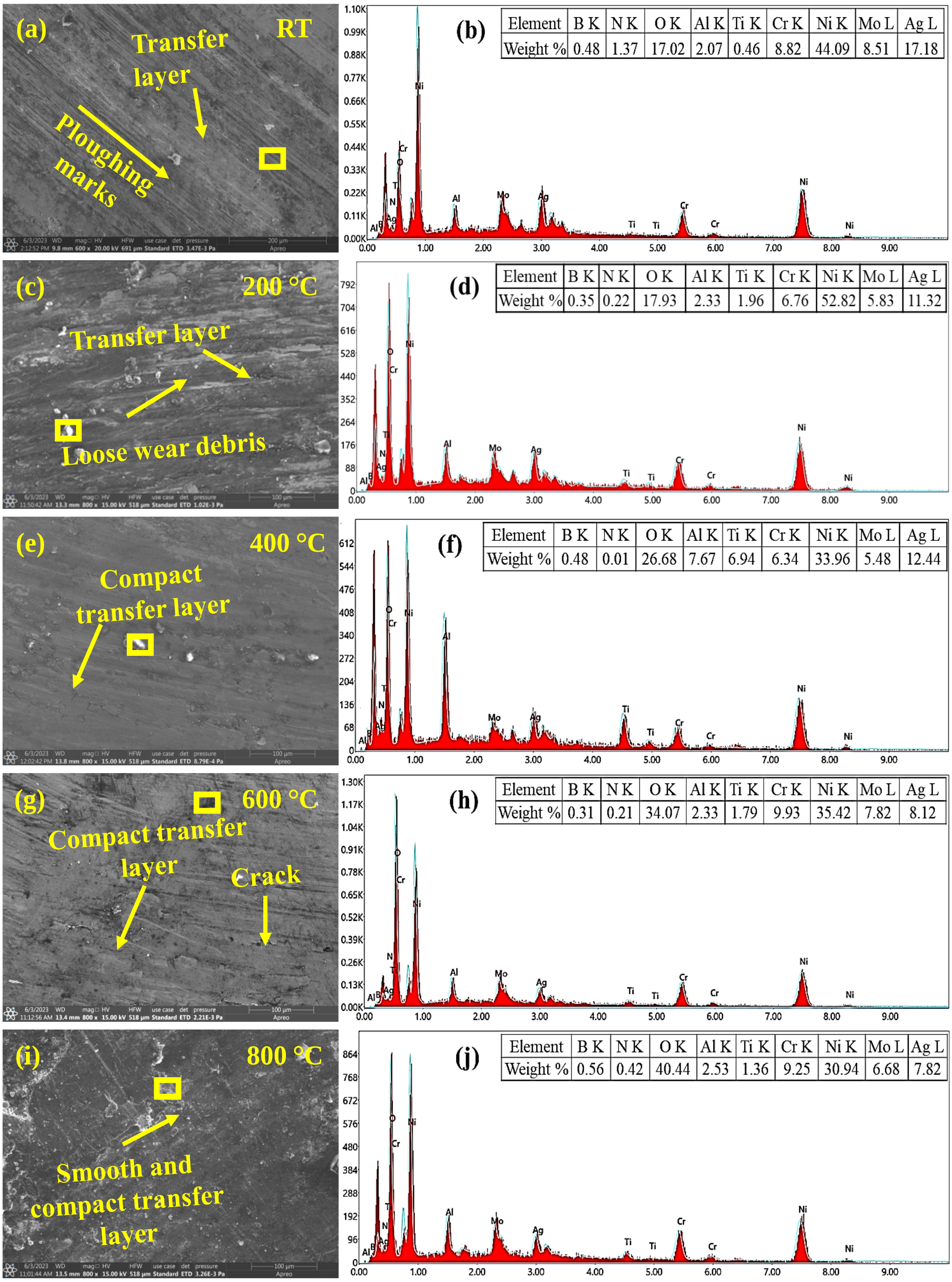

(b)

Element	B K	N K	O K	Al K	Ti K	Cr K	Ni K	Mo L	Ag L
Weight %	0.48	1.37	17.02	2.07	0.46	8.82	44.09	8.51	17.18

(d)

Element	B K	N K	O K	Al K	Ti K	Cr K	Ni K	Mo L	Ag L
Weight %	0.35	0.22	17.93	2.33	1.96	6.76	52.82	5.83	11.32

(f)

Element	B K	N K	O K	Al K	Ti K	Cr K	Ni K	Mo L	Ag L
Weight %	0.48	0.01	26.68	7.67	6.94	6.34	33.96	5.48	12.44

(h)

Element	B K	N K	O K	Al K	Ti K	Cr K	Ni K	Mo L	Ag L
Weight %	0.31	0.21	34.07	2.33	1.79	9.93	35.42	7.82	8.12

(j)

Element	B K	N K	O K	Al K	Ti K	Cr K	Ni K	Mo L	Ag L
Weight %	0.56	0.42	40.44	2.53	1.36	9.25	30.94	6.68	7.82

Fig. 6. 15 FESEM micrographs of the worn-out NAh4 composite and EDS of the marked region at (a and b) RT, (c and d) 200, (e and f) 400, (g and h) 600, and (i and j) 800 °C

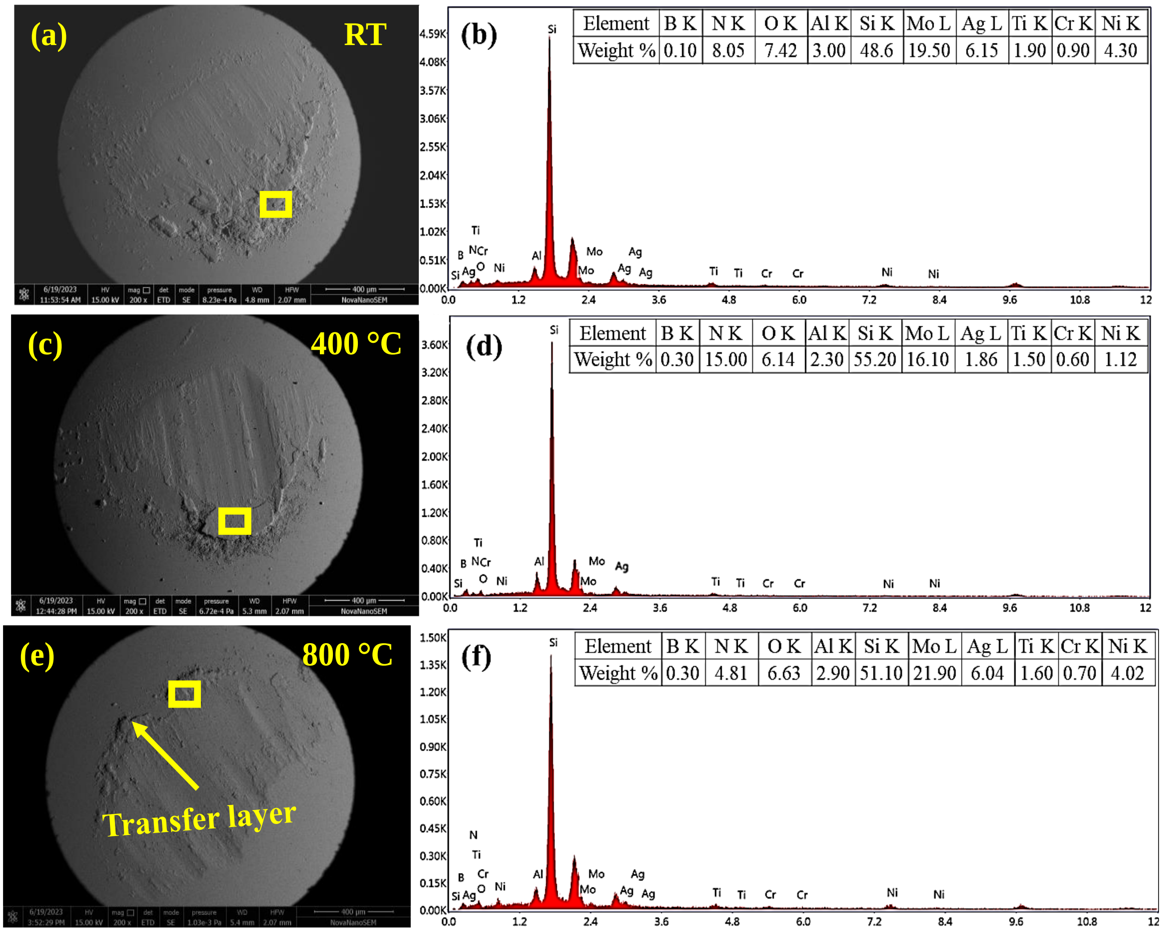

(b)

Element	B K	N K	O K	Al K	Si K	Mo L	Ag L	Ti K	Cr K	Ni K
Weight %	0.10	8.05	7.42	3.00	48.6	19.50	6.15	1.90	0.90	4.30

(d)

Element	B K	N K	O K	Al K	Si K	Mo L	Ag L	Ti K	Cr K	Ni K
Weight %	0.30	15.00	6.14	2.30	55.20	16.10	1.86	1.50	0.60	1.12

(f)

Element	B K	N K	O K	Al K	Si K	Mo L	Ag L	Ti K	Cr K	Ni K
Weight %	0.30	4.81	6.63	2.90	51.10	21.90	6.04	1.60	0.70	4.02

Fig. 6. 16 FESEM micrographs of the worn-out silicon nitride ball (counterface) slid against NAh4 along with EDS at the marked region at (a and b) RT, (c and d) 400, and (e and f) 800 °C

The FESEM micrographs of the worn surfaces of NAh6 at RT, 200, 400, 600, and 800 °C, along with the EDS analyses at 800 °C, are shown in Figs. 6.17 (a-j). The presence of a transfer layer along with ploughing marks can be seen on the worn surface of NAh6 after sliding at RT (Fig. 6.17 (a)). One may observe the transfer layer having different degrees of compaction on the worn surfaces at 200 and 400 °C, whereas some delamination on the transfer layer can be seen on the worn surface at 600 °C (Figs. 6.17 (b-d)). The presence of loose wear debris and a compact transfer layer could be observed on the worn surface of NAh6 at 800 °C as seen from Fig. 6.17 (e). The EDS analyses of the square regions marked in Figs. 6.17 (a, c, e, g, and i) reveal the presence of constituent elements of the composite and oxygen along with their respective amounts depending on the temperature indicating towards the possibility of oxidation as evident from 6.17 (b, d, f, h, and j).

The morphology of the worn surfaces of the ball slid against NAh6 at RT, 400, and 800 ºC and their EDS analyses are depicted in Figs. 6.18 (a-f). The worn surface at RT shows the wear scar with presence of very little wear debris at the edges as seen from Fig. 6.18 (a). The surfaces worn at 400 and 800 ºC show a discontinuous or scattered layer of compacted debris as seen from Fig. 6.18 (c) and (e), respectively. However, the layer appears to be covering a relatively large area of wear scar at 400 than at 800 ºC. The EDS analysis of the regions marked by square on the worn surface of the ball given in Figs. 6.18 (b, d, and f) reveal the transfer of material from the composite to the ball and the presence of oxygen pointing toward the oxidation of elements.

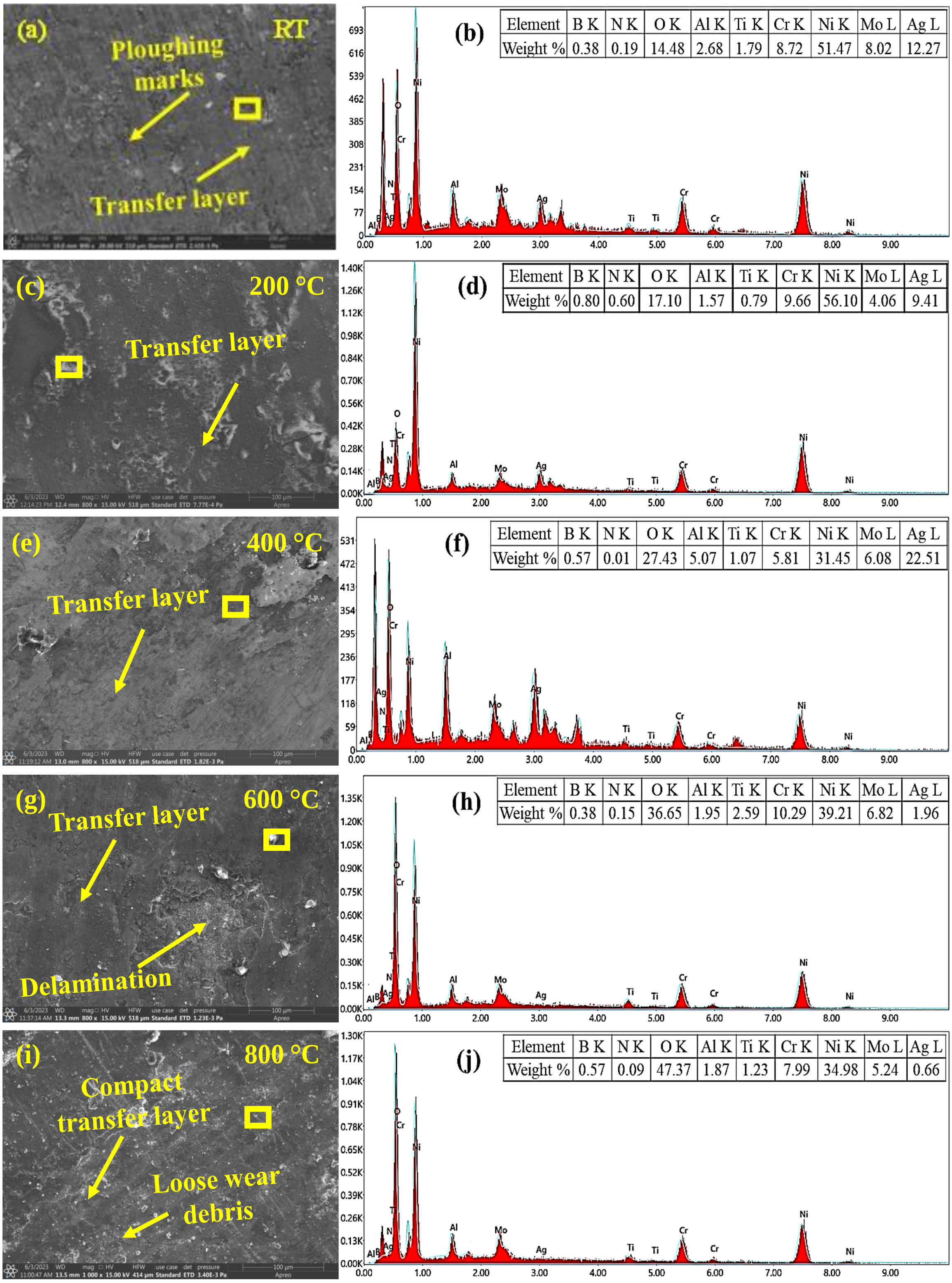

(b)

Element	B K	N K	O K	Al K	Ti K	Cr K	Ni K	Mo L	Ag L
Weight %	0.38	0.19	14.48	2.68	1.79	8.72	51.47	8.02	12.27

(d)

Element	B K	N K	O K	Al K	Ti K	Cr K	Ni K	Mo L	Ag L
Weight %	0.80	0.60	17.10	1.57	0.79	9.66	56.10	4.06	9.41

(f)

Element	B K	N K	O K	Al K	Ti K	Cr K	Ni K	Mo L	Ag L
Weight %	0.57	0.01	27.43	5.07	1.07	5.81	31.45	6.08	22.51

(h)

Element	B K	N K	O K	Al K	Ti K	Cr K	Ni K	Mo L	Ag L
Weight %	0.38	0.15	36.65	1.95	2.59	10.29	39.21	6.82	1.96

(j)

Element	B K	N K	O K	Al K	Ti K	Cr K	Ni K	Mo L	Ag L
Weight %	0.57	0.09	47.37	1.87	1.23	7.99	34.98	5.24	0.66

Fig. 6. 17 FESEM micrographs of the worn-out NAh6 composite and EDS of the marked region at (a and b) RT, (c and d) 200, (e and f) 400, (g and h) 600, and (i and j) 800 °C

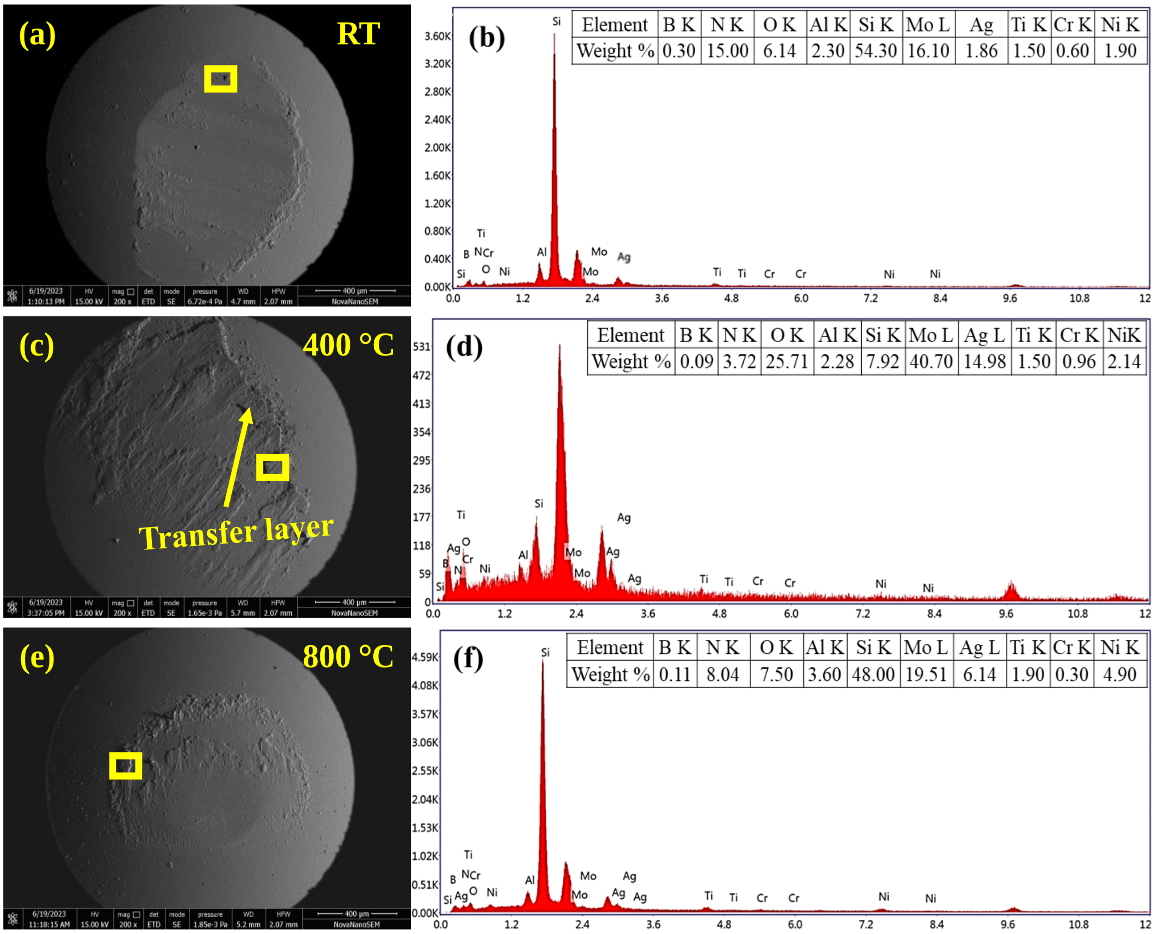

Element	B K	N K	O K	Al K	Si K	Mo L	Ag	Ti K	Cr K	Ni K
Weight %	0.30	15.00	6.14	2.30	54.30	16.10	1.86	1.50	0.60	1.90

Element	B K	N K	O K	Al K	Si K	Mo L	Ag L	Ti K	Cr K	NiK
Weight %	0.09	3.72	25.71	2.28	7.92	40.70	14.98	1.50	0.96	2.14

Element	B K	N K	O K	Al K	Si K	Mo L	Ag L	Ti K	Cr K	Ni K
Weight %	0.11	8.04	7.50	3.60	48.00	19.51	6.14	1.90	0.30	4.90

Fig. 6. 18 FESEM micrographs of the worn-out silicon nitride ball (counterface) slid against NAh6 along with EDS at the marked region at (a and b) RT, (c and d) 400, and (e and f) 800 °C

Figures 6.19 (a-j) present the morphology of the surface of NAh8 worn at RT, 200, 400, 600, and 800 °C as examined under FESEM along with their EDS analyses. The presence of a transfer layer along with ploughing marks is observed on the surface of NAh8 worn at RT as seen in Fig. 6.19 (a) whereas loose wear particles could be seen at 200 °C apart from a scattered transfer layer as depicted in Fig. 6.19 (c). The surface worn at 400 °C shows the presence of a smooth transfer layer only with no wear particles, while the worn surface at 600 °C exhibits a smooth layer with presence of loose wear debris as shown in Figs. 6.19 (e and g). However, the transfer layer appears to be cracking at a few locations as marked by arrows in Figs. 6.19 (e and g). One may observe the presence of a scattered transfer layer with some signs of delamination on the surface of NAh8 worn at 800 °C as seen from Fig. 6.19 (i). Again, the EDS analyses of the square regions marked in Figs. 6.19 (a, c, e, g, and i) reveal the presence of constituent elements of the composite and oxygen as evident from Figs. 6.19 (b, d, f, h, and j).

The micrographs of the worn surfaces of the ball slid against NAh8 at RT, 400, and 800 °C and their EDS analyses are illustrated in Figs. 6.20 (a-f). The worn surface at RT shows the wear scar with presence of very little wear debris at the edges as seen from Fig. 6.20 (a) whereas the surface worn at 400 °C shows the presence of relatively more debris at the edge as seen from Fig. 6.20 (c). However, one may observe the presence of a discontinuous or scattered layer of debris on the surface of ball worn at 800 °C as seen from Fig. 6.20 (e). The EDS analysis of the regions marked by square on the worn surface of the ball given in Figs. 6.20 (b, d, and f) reveal the transfer of material from the composite to the ball and the presence of oxygen.

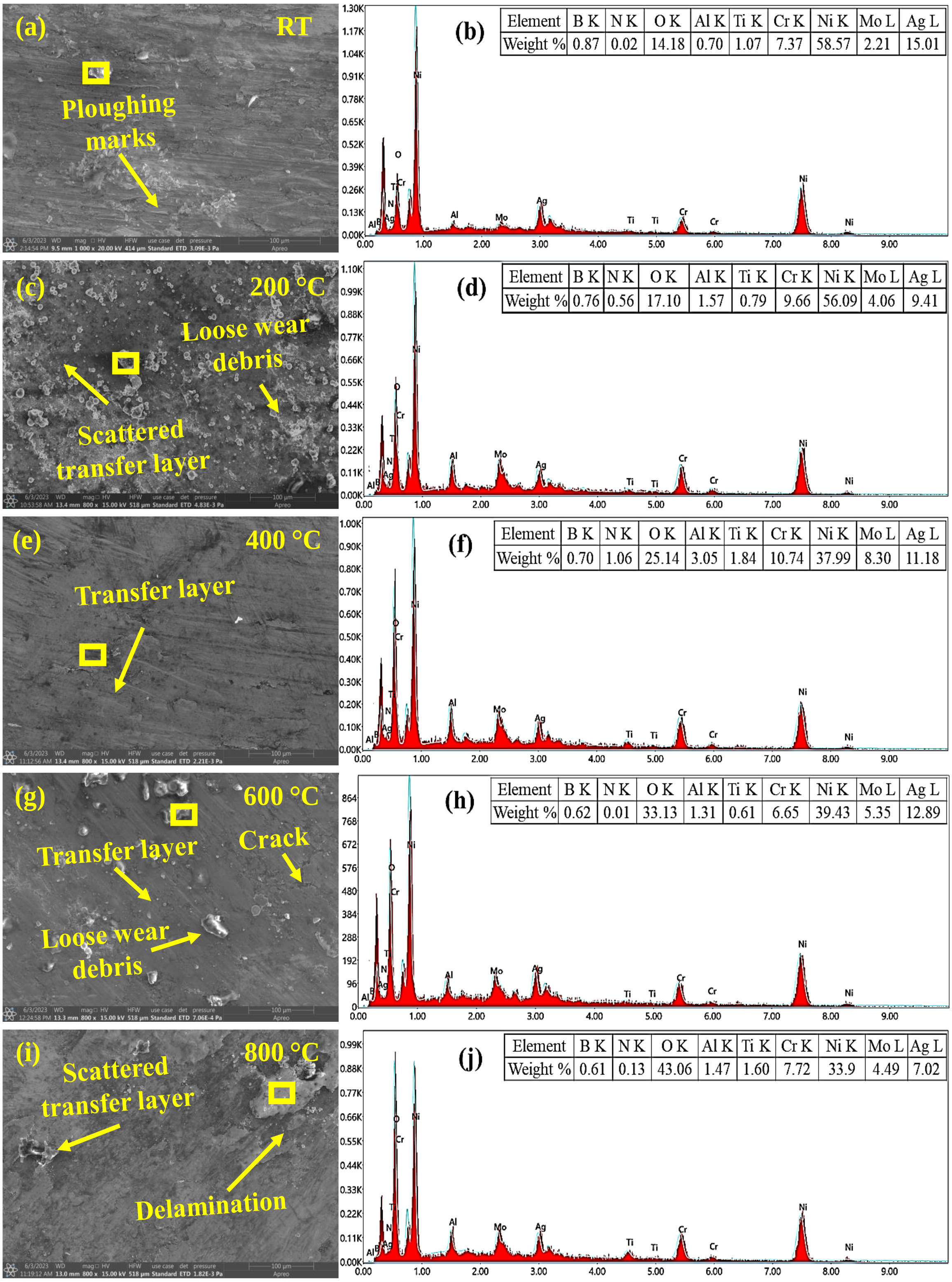

(b)

Element	B K	N K	O K	Al K	Ti K	Cr K	Ni K	Mo L	Ag L
Weight %	0.87	0.02	14.18	0.70	1.07	7.37	58.57	2.21	15.01

(d)

Element	B K	N K	O K	Al K	Ti K	Cr K	Ni K	Mo L	Ag L
Weight %	0.76	0.56	17.10	1.57	0.79	9.66	56.09	4.06	9.41

(f)

Element	B K	N K	O K	Al K	Ti K	Cr K	Ni K	Mo L	Ag L
Weight %	0.70	1.06	25.14	3.05	1.84	10.74	37.99	8.30	11.18

(h)

Element	B K	N K	O K	Al K	Ti K	Cr K	Ni K	Mo L	Ag L
Weight %	0.62	0.01	33.13	1.31	0.61	6.65	39.43	5.35	12.89

(j)

Element	B K	N K	O K	Al K	Ti K	Cr K	Ni K	Mo L	Ag L
Weight %	0.61	0.13	43.06	1.47	1.60	7.72	33.9	4.49	7.02

Fig. 6. 19 FESEM micrographs of the worn-out NAh8 composite and EDS of the marked region at (a and b) RT, (c and d) 200, (e and f) 400, (g and h) 600, and (i and j) 800 °C

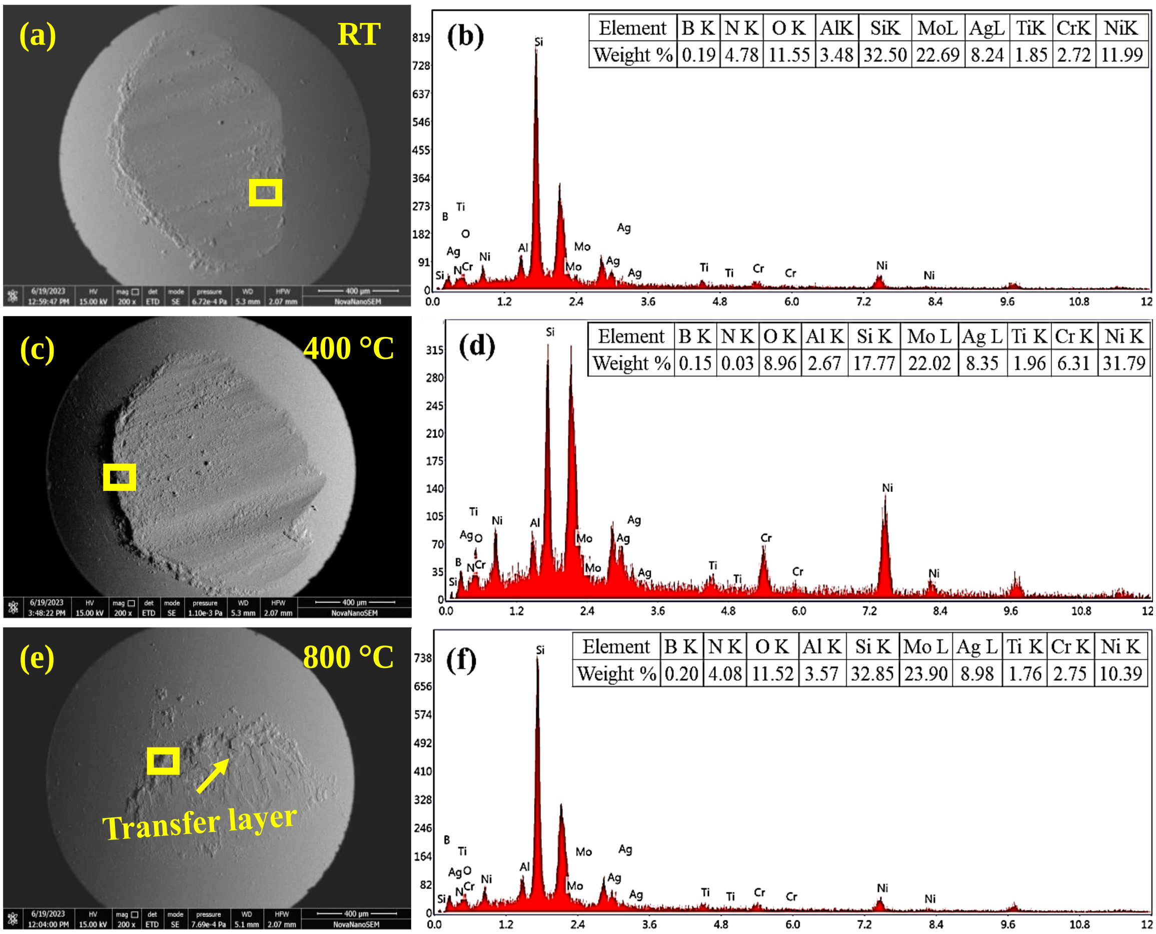

Element	B K	N K	O K	AlK	SiK	MoL	AgL	TiK	CrK	NiK
Weight %	0.19	4.78	11.55	3.48	32.50	22.69	8.24	1.85	2.72	11.99

Element	B K	N K	O K	Al K	Si K	Mo L	Ag L	Ti K	Cr K	Ni K
Weight %	0.15	0.03	8.96	2.67	17.77	22.02	8.35	1.96	6.31	31.79

Element	B K	N K	O K	Al K	Si K	Mo L	Ag L	Ti K	Cr K	Ni K
Weight %	0.20	4.08	11.52	3.57	32.85	23.90	8.98	1.76	2.75	10.39

Fig. 6. 20 FESEM micrographs of the worn-out silicon nitride ball (counterface) slid against NAh8 along with EDS at the marked region at (a and b) RT, (c and d) 400, and (e and f) 800 °C

6.1.3.2 X-ray diffraction analysis of worn surface of composites

The X-ray diffraction patterns of the worn surface of the composites, i.e., NA, NAh2, NAh4, NAh6, NAh8, and base alloy (N0) at RT, 200, 400, 600 and 800 °C, respectively, are shown in Figs. 6.21 (a-e). XRD pattern of the worn surface of N0 at RT (Fig. 6.21 (a)) reveals the existence of peaks corresponding to NiCr (ICSD 98-010-2819), NiAl (ICSD 98-060-4356), and NiTi (ICSD 98-016-6010) whereas additional peaks corresponding to Ag (ICSD 01-087-0598) could be seen for the composite NA containing 10 wt. % Ag. However, the composites namely, NAh2, NAh4, NAh6, and NAh8 exhibit extra peaks of *h*-BN (ICSD 01-085-1068) along with the peaks of NiCr, NiAl, NiTi, and Ag phases. The presence of the same diffraction peaks for base alloy and composites as seen at RT could also be observed at 200 °C, as evidenced from Figs. 6.21 (a and b). The XRD pattern of N0 at 400 °C given in Fig. 6.21 (c) demonstrates the presence of peaks corresponding to NiO (ICSD 98-009-2129), MoO_3 (ICSD 00-021-0569), and $NiMoO_4$ (ICSD 98-017-4488). One may observe the presence of additional peaks corresponding to Ag and *h*-BN in composites depending on composition as seen in Fig. 6.21 (c). However, the presence of a new peak corresponding to $NiTiO_3$ (ICSD 98-007-9285) in XRD pattern of N0 at 600 °C and few additional peaks pertaining to $NiTiO_3$, $Ag_2Mo_2O_7$ (ICSD 00-021-1339), and Ag_2MoO_4 (ICSD 00-008-473) in the XRD patterns of all the composites at 600 °C could be seen as illustrated in Fig. 6.21 (d). A similar pattern of peaks in XRD spectra for base alloy and composites is also seen at 600 and 800 °C (Figs. 6.21 (d and e)).

6.1.3.3 *Raman analysis of worn surface of composites*

The micro-Raman spectra of the worn surfaces of N0, NA, NAh2, NAh4, NAh6, and NAh8 at different temperatures, i.e., RT, 200, 400, 600, 800 °C, are depicted in Figs. 6.22 (a-d). Raman spectra for N0 and NA at RT (Fig. 6.22 (a)) illustrate the presence of a peak corresponding to Al_2O_3, whereas an additional peak of *h*-BN could be seen for NAh2, NAh4, NAh6, and NAh8. A similar pattern of peaks with additional peak of $NiMoO_4$ for base alloy and composites can be observed at 200 °C as illustrated in Figs. 6.22 (b). The Raman pattern for base alloy and composites is similar at 200 and 400 °C as seen from Figs. 6.22 (b and c). Raman spectra of the worn surface of base alloy (N0) at 600 °C reveals the presence of peaks corresponding to NiO, MoO_3, Cr_2O_3, $NiCr_2O_4$, $NiMoO_4$, Al_2O_3 as shown in Fig. 6.22 (d). The additional peaks of Ag_2MoO_4 and $Ag_2Mo_2O_7$ could be observed in the spectra of the worn surface of NA. However, extra peaks pertaining to *h*-BN could be seen in the spectrum of composites i.e., NAh2, NAh4, NAh6, and NAh8) at 600 °C apart from those observed for NA. The Raman spectra for the worn surfaces of base alloy as well as composites show the presence of similar peaks at 800 °C as observed in the spectra belonging to 600 °C as seen from Figs 6.22 (d and e).

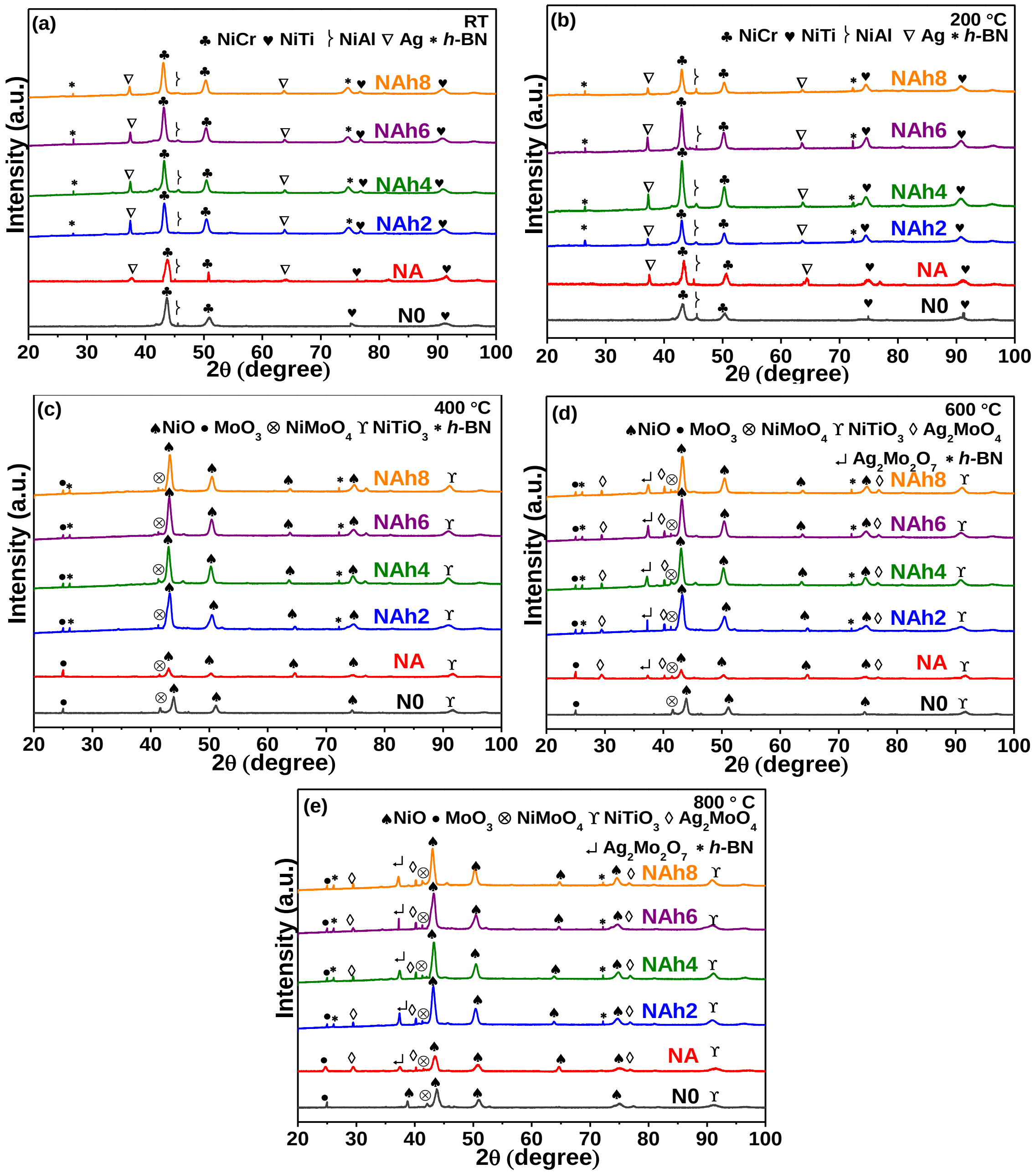

Fig. 6. 21 X-ray diffraction patterns of worn base alloy and composites at (a) RT, (b) 200, (c) 400, (d) 600, and (e) 800 °C

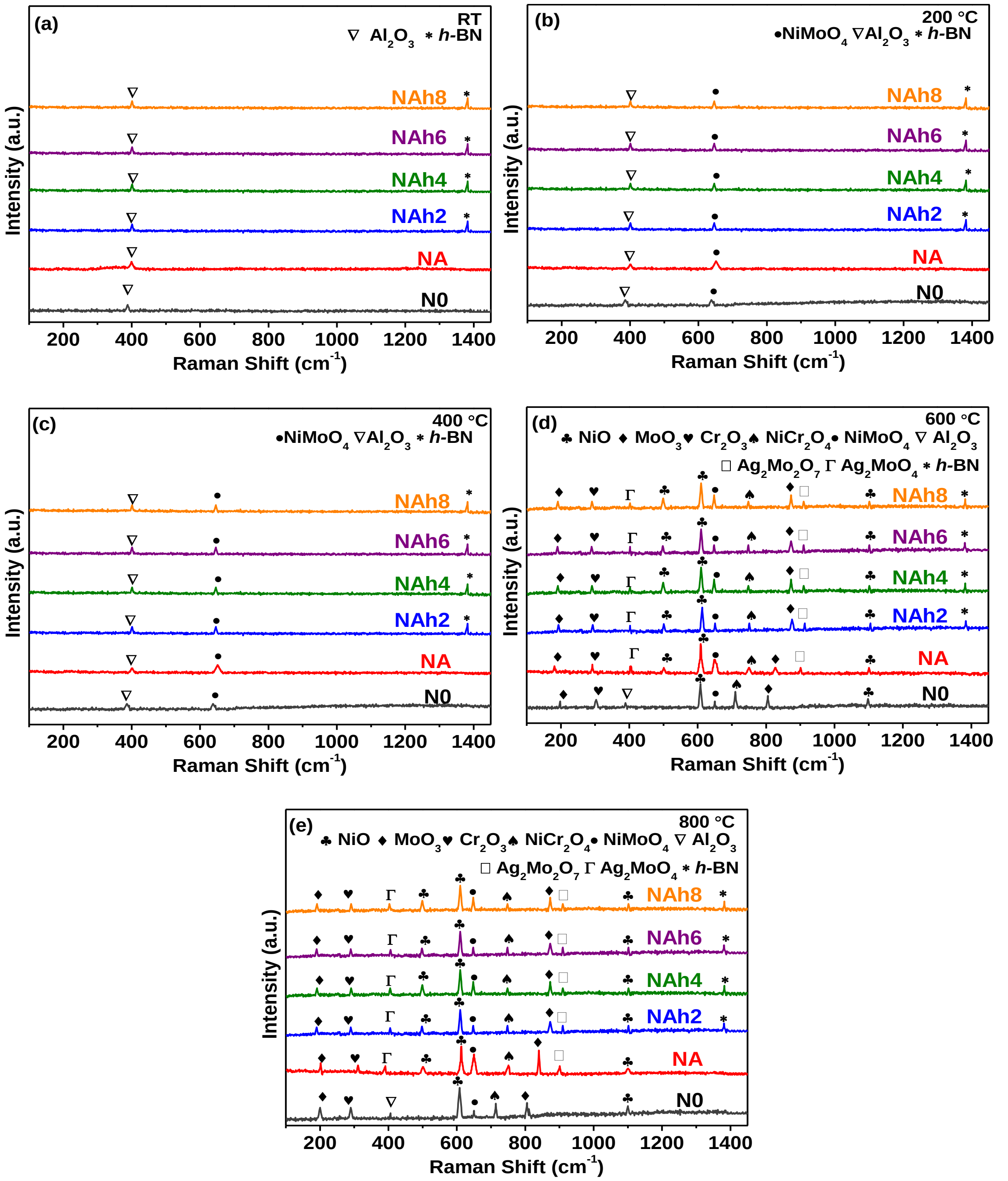

Fig. 6. 22 Raman spectra of worn base alloy and composites at (a) RT, (b) 200, (c) 400, (d) 600, and (e) 800 ºC

6.1.3.4 Examination of Subsurface

FESEM images of the subsurface for NAh2, NAh4, NAh6, and NAh8, worn at 800°C are given as Figs. 6.23 (a-d) confirm the presence of a tribo-layer. The average thickness of tribo-layer for NAh2, NAh4, NAh6, and NAh8 has been found to be 143.1, 150.5, 169.4, and 179.0 μm, respectively.

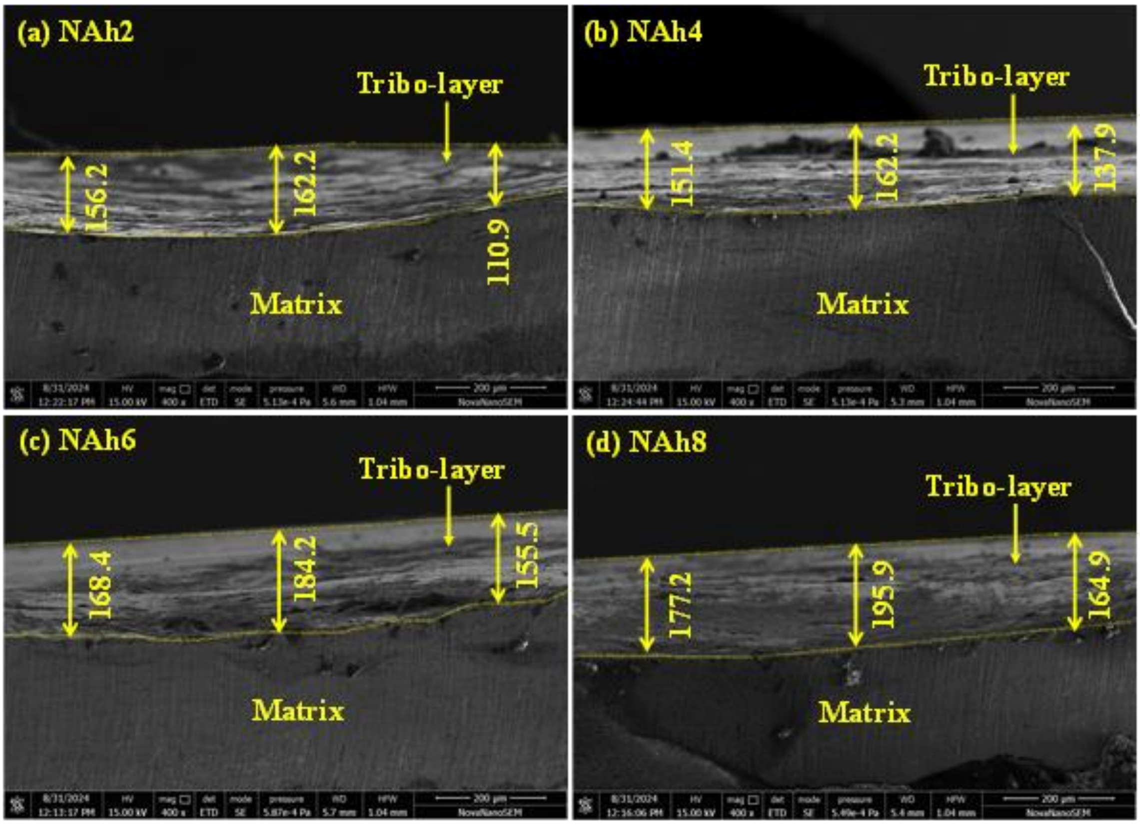

Fig. 6. 23 Cross-sectional FESEM micrographs of the worn subsurface at 800 °C corresponding to (a) NAh2, (b) NAh4, (c) NAh6, and (d) NAh8

6.2 DISCUSSION

The hardness of Ni alloy gets reduced by the addition of Ag due to the intrinsic softness of Ag as reported by earlier studies also [39,67]. The incorporation of 2, 4, 6, and 8 wt.% *h*-BN in addition to Ag brings about a further reduction in the hardness of the Ni alloy, which may be attributed to the poor sintering and wetting characteristics of *h*-BN despite the fact that *h*-BN has been modified by Ni with an aim to improve these features. The other contributing factor may be the agglomeration of *h*-BN in composites containing a relatively higher content viz. 6 and 8 wt. % *h*-BN as seen from Figs. 6.8 (e and f). A similar observation has also been reported by other researchers [41,114].

The initial fluctuations in the coefficient of friction (CoF) for base alloy (N0) and composites NA, NAh2, NAh4, NAh6, and NAh8 may be ascribed to the presence of asperities due to the initial surface roughness of the materials. The asperities get smoothened due to the continuous rubbing as the sliding progresses, and the surfaces attain better conformity with each other after a certain running-in period, resulting in the stabilisation of CoF, as seen in Fig. 6.10. The duration of the running-in period depends on the temperature and composition (in turn on the hardness) of material.

The observed friction and wear behaviour of base alloy (N0), NA, NAh2, NAh4, NAh6, and NAh8 with composition at a particular temperature (Figs. 6.11 and 6.12) may be explained on the basis of features such as the presence of loose wear particles, a transfer layer comprising elements from ball/composite, their oxides, and lubricious compounds on the worn surface of the composites at different temperatures apart from the hardness of the material. The loose wear particles cause abrasion, leading to a relatively higher loss of material, or may form a transfer film over the worn surface of the composite. The transfer film may either be continuous, covering the larger area of the worn surface, which inhibits the direct contact between mating bodies, leading to a smaller loss of material, or scattered, allowing the contact at some places with the counter-face asperities, resulting in larger loss of material as well as friction. The transfer film may either be compact and smooth, which effectively shields the underlying substrate from direct contact with the counterface, resulting in low friction and wear, or loosely bound, which may increase friction and wear. The tribological performance of a tribo-pair is controlled by the relative dominance of several dynamic processes such as softening of the material, formation of new compounds and oxides, strain hardening (which may occur at room temperature and can cause an increase in hardness), presence of the transfer layer and its nature, taking place during sliding at different temperatures. The hardness and wear rate possess an inverse relationship, as stated by Archard [28]. The hardness of the material has been shown to decrease with increasing temperature due to softening, hence the wear rate may increase [95,115]. On the other hand, the formation of a tribo-layer containing the lubricous species results in a decrease in both friction and wear as this layer provides easy-to-shear junctions at the sliding interface. Another important factor affecting the friction and wear performance of self-lubricating composites is the occurrence of synergistic action between the added lubricants. However, the final performance depends on the relative domination of the various competitive processes occurring during sliding conditions.

The observed variation of average CoF with temperature for both N0 and NA was already discussed thoroughly in section 4.12, on the basis of the features present on their worn surfaces such as existence of loose wear particles, nature of the transfer layer and its delamination, the presence of lubricious species, the X-ray diffraction and the Raman spectroscopy depending on the test temperature. Hence, details are not provided here.

The existence of deep ploughing marks on the surface of NAh2 worn at RT as shown in Fig. 6.13 (a), might be responsible for higher CoF at RT in comparison to other temperatures, i.e., 200, 400, 600, and 800 ºC as depicted in Fig. 6.10, despite a relatively larger coverage provided by the transfer layer. Nevertheless, a notable reduction in CoF for NAh2 from RT to 200 ºC followed by a slight reduction afterwards till 600 ºC may be ascribed to the presence of relatively shallow ploughing marks and the nature of the transfer layers at 200, 400, and 600 ºC as shown in Figs. 6.13 (c, e, and g). However, the presence of a relatively smooth and compact transfer layer with no discernible ploughing marks on the surface worn at 800 ºC compared to the one observed at 600 ºC as seen from the comparison of Figs 6.13 (g and i) might have reduced the CoF significantly from 600 to 800 ºC by inhibiting the direct contact between the mating bodies. The transfer layers have been found to consist of *h*-BN and other lubricious oxides such as NiO, MoO_3, $NiMoO_4$, $NiCr_2O_4$ Ag_2MoO_4 and $Ag_2Mo_2O_7$ [33,39,42,61] at 200, 400, 600, and 800 ºC as confirmed by XRD and Raman spectra of NAh2 shown in Figs. 6.21 (b-e) and 6.22 (b-e), respectively. The presence of oxides as determined by XRD and Raman spectra also confirms the oxidation of constituent elements which we speculated due to the presence of oxygen in EDS analyses given in Figs. 6.13 (b, d, f, h, and j). The presence of lubricous species provides the low shearing ability at the interface whereas a well compacted and continuous transfer layer avoids the direct contact between tribo-pair depending on its area coverage. Both of these conditions are conducive to a reduction in the CoF. The increase in wear rate from RT to 400 ºC with a significant rise between 200 and 400 ºC as shown in Fig. 6.12, may be attributed to the existence of loose wear debris, which might have caused abrasion despite the presence of a transfer layer containing lubricious compounds on the worn surface of NAh2 (Figs. 6.13 (a, c, and e) and ball (Figs. 6.14 (b and d). However, a reduction in wear rate from 400 to 800 ºC with a sharp decrease from 600 to 800 ºC may be ascribed to the presence of a well compacted and continuous transfer layer containing lubricious oxides of Ni and Mo apart from *h*-BN and silver molybdates on the contact surface of NAh2 (Figs. 6.13 (g and i)) and ball (Fig. 6.14 (c and e) as seen from EDS analysis and confirmed by XRD and Raman spectra of NAh2 as described above.

The relatively higher CoF of NAh4 at RT compared to other temperatures, i.e., 200, 400, 600, and 800 ºC (Fig. 6.11), may be credited to the presence of a transfer layer along with ploughing marks on the surface of NAh4 worn at RT as shown in Fig. 6.15 (a). Nevertheless, a notable reduction in CoF for NAh4 from RT to 400 ºC could be ascribed to the presence of transfer layers on the surfaces worn with increasing degree of compaction with rising temperature. A slight decrease in CoF from 400 to 600 ºC and a sharp decreased thereafter till 800 ºC may again be ascribed to the larger degree of compaction of the transfer layers on the surfaces at relatively higher temperatures as seen from a comparison of Figs. 6.15 (a, c, e, g, and i). The transfer layers have been found to contain lubricious species such as Ag, *h*-BN, NiO, MoO_3, $NiMoO_4$, $NiCr_2O_4$ Ag_2MoO_4, and $Ag_2Mo_2O_7$ depending on temperatures as confirmed by EDS analyses, XRD and Raman spectra of NAh4 shown in Figs. 6.15 (b, d, f, h, and j), 6.21 (b-e), and 6.22 (b-e), respectively. The presence of a smooth and compact transfer layers containing lubricious species reduces the CoF by providing low shearing junctions at the interface, as described earlier. The increase in wear rate from RT to 400 ºC with a sharp increase from 200 to 400 ºC as shown in Fig. 6.12, may be attributed to the incidence of loose wear debris, which might have caused abrasion despite the presence of a transfer layer containing lubricious compounds on the worn surface of NAh4 (Figs. 6.15 (a, c, and e) and ball (Figs. 6.16 (b and d). However, a reduction in wear rate from 400 to 800 ºC with a sharp decline from 600 to 800 ºC may be ascribed to the presence of a compact and continuous transfer layer containing lubricious oxides of Ni and Mo apart from *h*-BN and silver molybdates on the contact surface of NAh4 (Figs. 6.15 (g and i)) and ball (Figs. 6.16 (c and e) as seen from EDS analysis and confirmed by XRD and Raman spectra of NAh4 shown in Figs. 6.15 (h and j), 6.16 (h and j), 6.21 (d and e), and 6.22 (d and e), respectively.

A consistent decrease in CoF with increasing temperature from RT to 800 ºC for NAh6 as observed in Fig. 6.11, may again be explained on the basis of the comparison of features i.e., nature of transfer layer whether compact/loosely or continuous/scattered, the area coverage of the transfer layer and lubricating compounds present on the surfaces worn at these temperatures. A relatively sharp reduction in CoF for NAh6 from RT to 200 ºC, a slight reduction between 200 and 600 ºC and a sharp decrease from 600 to 800 ºC may be attributed to the presence of transfer layers at 200, 400, 600, and 800 ºC with increasing area coverage and degree of compaction with increasing temperature as seen in Figs. 6.17 (a, c, e, g, and i). A transfer layer with a larger coverage and higher degree of compaction helps in reducing adhesion between mating bodies and results in a decrease in CoF. The availability of lubricious species in the transfer layers, which has been confirmed by XRD and Raman analysis for NAh6 as seen from Figs. 6.21 and 6.22, respectively, also contributed to decreasing CoF with increasing temperature. The increase in wear rate from RT to 400 ºC with a significant rise from 200 to 400 ºC as seen from Fig. 6.12 may be attributed to the abrasive action of loose wear particles present on the worn surface despite the presence of a transfer layer containing lubricious compounds on the worn surface of NAh6 (Figs. 6.17 (a, c, and e) and ball (Figs. 6.18 (a and c). However, a reduction in wear rate from 400 to 800 ºC with a sharp decrease from 600 to 800 ºC may be ascribed to the presence of a compact and continuous transfer layer containing lubricious species on the worn surface of NAh6 (Figs. 6.17 (g and i)) and ball (Fig. 6.18 (e) as seen from EDS analyses and confirmed by XRD and Raman spectra of NAh6 shown in Figs. 6.17 (h and j), 6.19 (h and j), 6.20 (d and e), and 6.21(d and e), respectively.

The relatively high CoF for NAh8 at RT and 200 ºC in comparison to CoF at 400, 600, and 800 ºC as seen in Fig. 6.11 may again be explained on the basis of the morphological features of the worn surfaces at these temperatures. The presence of a transfer layer covering a larger area apart from loose wear debris on the surface worn at 200 ºC in comparison to that at RT might have caused a slight decrease in CoF as seen in Figs. 6.18 (a and c). The presence of a transfer layer covering almost the entire surface worn at 400 and 600 ºC as seen from Fig. 6.18 (e), might have played a role in significantly reducing the CoF from 200 to 600 ºC. A sharp decrease from 600 to 800 ºC may be credited to the enhanced compaction of the transfer layer due to higher temperature as evident from a comparison of Figs. 6.18 (e and g). A well-compacted layer with a larger coverage assists in reducing the CoF as explained earlier. The availability of lubricious species confirmed by XRD and Raman analysis for NAh8 as seen in Figs. 6.20 and 6.21, respectively, might have also contributed to diminishing CoF. The increase in wear rate from RT to 400 ºC as seen from Fig. 6.12, might be due to the abrasive action of loose wear particles on the worn surface of NAh8 (Figs. 6.18 (a, c, and e) and ball (Figs. 6.19 (a and c)) as indicated above. However, a reduction in wear rate from 400 to 800 ºC with a sharp decrease from 600 to 800 ºC can be attributed to the protection provided by the compact and continuous transfer layer having lubricious species on the surface of NAh8 worn at 800 ºC (Figs. 6.18 (g and i)) and ball (Fig. 6.19 (e) as seen from EDS analyses and confirmed by XRD and Raman spectra of NAh6 shown in Figs. 6.18, 6.19, 6.20 (b-d), and 6.21(b-e), respectively.

The decrease in CoF in composites NAh2, NAh4, NAh6, and NAh8 at all the temperatures, i.e., RT, 200, 400, 600, and 800 ºC, may be due to the increasing amount of *h*-BN. A comparative lower CoF shown by composites containing a combination of Ag and *h*-BN in comparison to that containing Ag only (NA) may be ascribed to the occurrence of a synergistic action between Ag and *h*-BN wherein Ag, being a low-temperature lubricant is assisted by *h*-BN which is considered an excellent high temperature lubricant having good thermal stability as indicated earlier by other authors also [42,116]. The occurrence of synergistic action can be established from the observed lower CoFs in composites containing both Ag and *h*-BN in comparison to the one containing only Ag at all the test temperatures. The addition of silver in base alloy results in reduced friction due to the presence of Ag at temperatures till 400 ºC and its molybdates at 600 and 800 ºC. The increase in the thickness of the transfer layer on the worn surface of the composites with increase in the amount of *h*-BN from 2 to 8 wt.% at 800 ºC as evidenced by Figs. 6.22 (a-d) might also have contributed in lowering down the CoF.

The increase in specific wear rate of NAh2, NAh4, NAh6, and NAh8 from RT to 400 ºC (Fig. 6.11) may again be explained on the basis of the softening of the surface with increasing temperature due to a decrease in hardness as reported by others also[35,36]. A consistently lower wear rate shown by the composites containing 2 and 4 wt.% *h*-BN, i.e., NAh2 and NAh4, in comparison to N0 and NA at all the temperatures, may be attributed to the characteristics of the transfer layer present on their worn surfaces apart from the synergistic action of Ag and *h*-BN reflecting the effectiveness of these over the reduced hardness. However, a higher wear rate observed for NAh6 and NAh8 containing 6 and 8 wt.% *h*-BN, respectively, may be due to the relatively lower hardness of these composites in comparison to N0 and NA caused by the agglomeration of *h*-BN despite the presence of the higher amount of lubricating agent. This indicates the dominance of the effect of hardness over the lubricating efficacy of lubricants in controlling the wear in these composites. The high potential contributing factor for the reduction in wear rate at 800 ºC might be the thickening of the transfer layer on the worn surface of the composites with an increased amount of *h*-BN at 800 ºC, as seen in Figs. 6.23 (a-d). Based on above analysis, the dominant wear mechanism for all the composites is ploughing at RT and a combination of abrasion and ploughing at 200 and 400 ºC, whereas it is oxidative at 600 and 800 ºC as revealed by the worn morphology.

To summarize, the composite NAh4 has shown the lowest wear rate, whereas NAh8 has shown the lowest CoF at all the temperatures among all the materials under the condition of load and sliding speed used in the present study. On the basis of the above discussion, we may conclude that one will have to prioritize between the two, i.e., either low friction or low wear, or strike a compromise between the two based on the intended application, while deciding the amount of addition of *h*-BN in the following composites.